Fundamental scales in the kinematic phase of the turbulent dynamo

Neco Kriel [1]*, James R. Beattie [1], Amit Seta [1], and Christoph Federrath [1,2]

[1]*Research School of Astronomy and Astrophysics, Australian National University, Canberra, Australia*
[2]*Australian Research Council Centre of Excellence in All Sky Astrophysics (ASTRO3D), Canberra, ACT 2611, Australia*

ABSTRACT

The turbulent dynamo is a powerful mechanism that converts turbulent kinetic energy to magnetic energy. A key question regarding the magnetic field amplification by turbulence, is, on what scale, k_p, do magnetic fields become most concentrated? There has been some disagreement about whether k_p is controlled by the viscous scale, k_ν (where turbulent kinetic energy dissipates), or the resistive scale, k_η (where magnetic fields dissipate). Here we use direct numerical simulations of magnetohydrodynamic turbulence to measure characteristic scales in the kinematic phase of the turbulent dynamo. We run 104-simulations with hydrodynamic Reynolds numbers of $10 \leqslant \mathrm{Re} \leqslant 3600$, and magnetic Reynolds numbers of $270 \leqslant \mathrm{Rm} \leqslant 4000$, to explore the dependence of k_p on k_ν and k_η. Using physically motivated models for the kinetic and magnetic energy spectra, we measure k_ν, k_η and k_p, making sure that the obtained scales are numerically converged. We determine the overall dissipation scale relations $k_\nu = (0.025^{+0.005}_{-0.006}) \, k_{\mathrm{turb}} \, \mathrm{Re}^{3/4}$ and $k_\eta = (0.88^{+0.21}_{-0.23}) \, k_\nu \, \mathrm{Pm}^{1/2}$, where k_{turb} is the turbulence driving wavenumber and $\mathrm{Pm} = \mathrm{Rm}/\mathrm{Re}$ is the magnetic Prandtl number. We demonstrate that the principle dependence of k_p is on k_η. For plasmas where $\mathrm{Re} \gtrsim 100$, we find that $k_p = (1.2^{+0.2}_{-0.2}) \, k_\eta$, with the proportionality constant related to the power-law 'Kazantsev' exponent of the magnetic power spectrum. Throughout this study, we find a dichotomy in the fundamental properties of the dynamo where $\mathrm{Re} > 100$, compared to $\mathrm{Re} < 100$. We report a minimum critical hydrodynamic Reynolds number, $\mathrm{Re}_{\mathrm{crit}} = 100$ for bonafide turbulent dynamo action.

Key words: dynamo – MHD – magnetic fields – turbulence

1 INTRODUCTION

The Universe is observed to be in a magnetised state on most astrophysical scales probed so far. This ranges from small scales, like planets (Stevenson 2010; Jones 2011; Sheyko et al. 2016) and stars (Choudhuri 2015; Beck & Wielebinski 2018), over the interstellar medium of galaxies (Beck 2001; Fletcher et al. 2011; Han 2017), through to scales occupied by the largest gravitationally bound structures in the Universe, galaxy clusters (Clarke et al. 2001; Brandenburg & Subramanian 2005; Vazza et al. 2014; Marinacci et al. 2018). Observing and probing these magnetic fields provide us with insight into the structure and dynamics of the astrophysical systems that they occupy, and the dynamically important roles that magnetic fields play (Subramanian 2016; Federrath 2016; Rincon 2019; Krumholz & Federrath 2019).

In the early Universe, magnetic fields were orders of magnitude weaker than they are observed to be in the present day, as most seed field generation mechanisms produce very weak magnetic fields (Grasso & Rubinstein 2001; Schleicher et al. 2010; Widrow et al. 2012; Durrer & Neronov 2013). While the origin of magnetic fields is still an unsolved problem, many theories predict weak magnetic fields of $\ll$ nG could be generated during various phases in the early Universe (see Subramanian 2016, and references therein). These magnetic fields are subject to resistive and turbulent decay, and in

spiral galaxies they are removed via other processes, such as galactic winds and flux expulsion (Weiss 1966; Gilbert et al. 2016; Seta 2019). To explain the observed magnetic fields of the present day, weak primordial magnetic fields therefore need to amplify on a timescale much faster than their dissipation and/or removal. Wagstaff et al. (2014) showed that the conditions for an efficient "turbulent dynamo" (also referred to as a small-scale dynamo in literature) to act in the early Universe are satisfied. The turbulent dynamo is the only mechanism capable of providing exponentially fast amplification of magnetic fields, explaining the μG fields observed in galaxies today (Widrow et al. 2012; Beck & Wielebinski 2018; Subramanian 2019). The main aim of this study is to determine on what scale magnetic fields become most concentrated, and how this magnetic peak scale (k_p) relates to the viscous (k_ν) and resistive (k_η) dissipation scales in the kinematic phase of the dynamo (Batchelor 1950; Kazantsev 1968; Kulsrud & Anderson 1992; Vainshtein & Cattaneo 1992; Schekochihin et al. 2002b, 2004b; Brandenburg & Subramanian 2005; Schober et al. 2015; Xu & Lazarian 2016; McKee et al. 2020).

1.1 A hierarchy of scales

Turbulence is associated with large hydrodynamic Reynolds numbers,

$$\mathrm{Re} \equiv \frac{\ell_{\mathrm{turb}} \, u_{\mathrm{turb}}}{\nu}, \tag{1}$$

---

* neco.kriel@anu.edu.au

where u_{turb} is the flow velocity on the driving scale ℓ_{turb}, and ν is the kinematic viscosity. The Re provides a measure of the ratio of inertial to viscous forces in a gas. At low Re, the viscous forces are dominant, and flows are laminar. Conversely, high Re flows are turbulent. The Re at which a flow transitions from laminar to turbulent depends on the geometry of the system, but fully developed turbulence generally develops for Re $\gtrsim$ 100–1000 (Frisch 1995; Schumacher et al. 2014).

For incompressible, homogeneous and isotropic turbulence, energy is transported from larger scales (where the turbulence is driven) to smaller scales (where the turbulent energy is dissipated by viscous forces). Eddies on length scale ℓ rotate with velocity $u_\ell \propto \ell/t_\ell \propto \ell^{1/3}$ (Kolmogorov 1941; Frisch 1995), where $t_\ell \propto \ell/u_\ell$ is the scale-dependent turnover time. Thus, the viscous scale for such a turbulent flow, $\ell_\nu \propto u_\nu^3$, is the scale where dissipation effects are dominant, and can be defined by the condition that the Reynolds number on ℓ_ν, Re_{ℓ_ν} is unity, i.e., $\text{Re}_{\ell_\nu} = \ell_\nu u_\nu/\nu \propto \ell_\nu^{4/3} \approx 1$. Thus, $\ell_\nu/\ell_{\text{turb}} \propto \text{Re}^{3/4}$, as per Equation 1, and the wavenumber associated with the viscous scale eddies is

$$k_\nu = \frac{2\pi}{\ell_\nu} \propto k_{\nu,\text{theory}} \equiv k_{\text{turb}} \, \text{Re}^{3/4}, \qquad (2)$$

where the turbulence driving wavenumber is $k_{\text{turb}} = 2\pi/\ell_{\text{turb}}$. Here, we use the symbol $\propto$ to emphasise that k_ν scales with $k_{\nu,\text{theory}}$, but may not be equal to it. In fact, one of our goals in this work is to determine k_ν and whether the theoretical dependence on $k_{\nu,\text{theory}} \equiv k_{\text{turb}} \, \text{Re}^{3/4}$ holds.

When magnetic fields are present, one can define the magnetic Reynolds number,

$$\text{Rm} \equiv \frac{\ell_{\text{turb}} \, u_{\text{turb}}}{\eta}, \qquad (3)$$

in analogy to the hydrodynamic Reynolds number (see Equation 1), where ν is replaced by the magnetic resistivity, η, and Rm is a measure of the ratio between induction forces and magnetic dissipation. The relative importance between ν and η can be quantified by the magnetic Prandtl number,

$$\text{Pm} \equiv \frac{\text{Rm}}{\text{Re}} = \frac{\nu}{\eta}. \qquad (4)$$

The Pm controls the scale separation between ℓ_ν and the resistive scale, ℓ_η, and is an important parameter for characterising the behaviour and evolution of the magnetic energy in a turbulent plasma. In the Pm $\gg$ 1 regime, Schekochihin et al. (2002b) provide an estimate for the resistive wavenumber as

$$k_\eta = \frac{2\pi}{\ell_\eta} \propto k_{\eta,\text{theory}} \equiv k_{\nu,\text{theory}} \, \text{Pm}^{1/2}. \qquad (5)$$

Here, we again use $\propto$ to emphasise that there may be a constant of proportionality between k_η and $k_{\eta,\text{theory}}$, to be determined in this study. This leads to a hierarchy of scales in the Pm > 1 regime, with $\ell_{\text{turb}} > \ell_\nu > \ell_\eta$. Here, $\ell_{\text{turb}} > \ell > \ell_\nu$ defines the inertial range of Kolmogorov turbulence, and $\ell_\nu > \ell > \ell_\eta$ defines the sub-viscous range.

Generally, in most astrophysical systems, Re and Rm are large, and therefore both velocity and magnetic fields are expected to be turbulent and span over a wide range of scales. However, while magnetic fields in astrophysical settings, like in the Milky Way, could have a wide range of scales available, it is of interest to know the scale, k_p, on which these fields are expected to become most concentrated. Batchelor (1950) argued that $k_p \propto k_\nu$, but more recent theories suggest that $k_p \propto k_\eta$ (Kazantsev 1968; Kulsrud & Anderson 1992; Vainshtein & Cattaneo 1992; Schekochihin et al. 2002b, 2004b; Brandenburg & Subramanian 2005; Schober et al. 2015; Xu

& Lazarian 2016; McKee et al. 2020). Our primary focus in this study is to determine the dissipation scales k_ν and k_η, and the magnetic peak scale k_p, and to compare our measurements with the theoretical predictions. We do so by utilising a suite of simulations of turbulent dynamo amplification, which span a large range of Re and Rm. In all of our simulations, we measure k_ν, k_η, and k_p, to test the theoretical relations given by Equation 2 and 5, and to determine the exact dependence of k_p on k_ν and k_η.

1.2 Magnetic field amplification

While the theory of turbulent magnetic field amplification dates back to Batchelor (1950) and Kazantsev (1968), and to many follow-up works (e.g., Brandenburg & Subramanian 2005; Federrath 2016; Rincon 2019), it is only within the last few years, that laboratory experiments have demonstrated that magnetic fields can be amplified by turbulent dynamo action (Meinecke et al. 2015; Tzeferacos et al. 2018; Bott et al. 2021). If initially the strength of the magnetic energy density, $E_{\text{mag}} = B^2/(8\pi)$, is much weaker than the turbulent kinetic energy density, $E_{\text{kin}} = \rho_0 \, u_{\text{turb}}^2/2$ (where ρ_0 is the mean gas density), then the turbulence is able to rapidly amplify the magnetic field (Batchelor 1950; Kazantsev 1968; Kulsrud & Anderson 1992; Vainshtein & Cattaneo 1992; Schekochihin et al. 2002b, 2004b; Brandenburg & Subramanian 2005; Schober et al. 2015; Xu & Lazarian 2016; Seta et al. 2020; McKee et al. 2020; Seta & Federrath 2021) by randomly stretching, twisting, and folding the magnetic field lines (Vainshtein et al. 1972; Zel'Dovich et al. 1984; Schekochihin et al. 2002b, 2004b; Seta et al. 2015). This is called the kinematic phase of the dynamo, with the condition that Rm exceeds a critical value, $\text{Rm}_{\text{crit}} \gtrsim 100$, depending on Pm and the level of compressibility (sonic Mach number) of the plasma (Schekochihin et al. 2004a,b; Haugen & Brandenburg 2004; Brandenburg & Subramanian 2005; Schober et al. 2012a; Federrath et al. 2014). The growth rate of the magnetic field has been shown to depend upon Re and Pm, with faster amplification associated with higher Re and Pm (Subramanian 1997; Schober et al. 2012a, 2015; Bovino et al. 2013; Federrath et al. 2014). Once the magnetic field becomes strong enough such that the Lorentz force exerts a significant back-reaction on the turbulent flow, the stretching motions (which amplify magnetic fields) are ultimately suppressed, the diffusion relative to stretching is enhanced, and both these processes combined lead to the saturation (saturated phase) of the turbulent dynamo (Schekochihin et al. 2002a; Seta et al. 2020; Seta & Federrath 2021).

The rest of the study is organised as follows. In §2 we introduce our numerical methods and simulation parameters. In §3 we present the results of this work, starting with the magnetic-to-turbulent kinetic energy ratio in §3.1. In §3.2 we investigate the morphology of the kinetic and magnetic energy during the kinematic phase of the dynamo. In §3.3 we analyse the velocity and magnetic field power spectra, and introduce our models and methods for measuring k_ν, k_η, and k_p from the spectra. In §3.5 we compare where we measure k_ν and k_η in our simulations with where theories predict these scales to be. In §3.6 and §3.7 we determine the dependence of k_p on the dissipation scales and link k_p to the slope of the magnetic field spectrum. In §4.1 and §4.2 we discuss the limitations and implications of the results within this study, respectively. Finally, we summarise this study and our results in §5.

2 NUMERICAL SIMULATIONS

2.1 MHD equations and numerical methods

We solve the compressible, non-ideal, magnetohydrodynamic (MHD) equations,

$$\frac{\partial \rho}{\partial t} + \nabla \cdot (\rho \boldsymbol{u}) = 0, \tag{6}$$

$$\rho \left(\frac{\partial}{\partial t} + \boldsymbol{u} \cdot \nabla \right) \boldsymbol{u} = \frac{1}{4\pi} (\boldsymbol{B} \cdot \nabla) \boldsymbol{B} - \nabla \left(p_{\text{th}} + \frac{B^2}{8\pi} \right)$$
$$+ \nabla \cdot (2\nu\rho \boldsymbol{S}) + \rho \boldsymbol{F}, \tag{7}$$

$$\frac{\partial \boldsymbol{B}}{\partial t} = \nabla \times (\boldsymbol{u} \times \boldsymbol{B}) + \eta \nabla^2 \boldsymbol{B}, \tag{8}$$

$$\nabla \cdot \boldsymbol{B} = 0, \tag{9}$$

for an isothermal plasma with constant kinematic viscosity, ν, and magnetic resistivity, η. In these equations, ρ is the gas density, $\boldsymbol{u}$ is the gas velocity, and $\boldsymbol{B} = \boldsymbol{B}_0 + \delta \boldsymbol{B}$ is the total magnetic field, which consists of a mean field, $\boldsymbol{B}_0$, (which we initialise as zero) and fluctuating, $\delta \boldsymbol{B}$, component (see §2.3 for details on how we initialise $\delta \boldsymbol{B}$). The viscous dissipation rate is included in the momentum equation (Equation 7) via the strain rate tensor $S_{ij} = (1/2) (\partial_i u_j + \partial_j u_i) + (2/3) \delta_{ij} \nabla \cdot \boldsymbol{u}$, where δ_{ij} is the Kronecker delta. $\boldsymbol{F}$ is the turbulent acceleration field, which we discuss in §2.2. We close the energy equation with an isothermal equation of state, $p_{\text{th}} = c_s^2 \rho$, where p_{th} is the thermal pressure, and c_s = const is the sound speed.

We use a modified version of the FLASH code (Fryxell et al. 2000; Dubey et al. 2008) to solve the MHD equations (Equation 6–9) on a uniformly discretised, triply periodic, three-dimensional grid with dimensions L^3. We test numerical convergence by running our simulations with different grid resolutions, with up to 576^3 grid cells (see §3.4 below). For solving the MHD equations, we use the five-wave, approximate Riemann solver described in Bouchut et al. (2007, 2010), and implemented and tested in Waagan et al. (2011).

2.2 Turbulence driving

The turbulent acceleration field, $\boldsymbol{F}$, in the momentum Equation 7 is modelled with an Ornstein-Uhlenbeck process (Eswaran & Pope 1988; Schmidt et al. 2009; Federrath et al. 2010). We use the Helmholtz decomposition of $\boldsymbol{F}$ to control the solenoidal (divergence-free) and compressive (curl-free) modes in $\boldsymbol{F}$ (Federrath et al. 2008, 2010). Here, we choose to drive with only solenoidal modes, because solenoidal driving is the most efficient at amplifying magnetic fields (Federrath et al. 2011, 2014; Martins Afonso et al. 2019; Chirakkara et al. 2021). We choose to work in the subsonic, near incompressible regime of turbulence, with Pm ⩾ 1, because the turbulent dynamo is most efficient in this regime (e.g., Schekochihin et al. 2004b, 2007; Schober et al. 2012a, 2015; Seta & Federrath 2020; Chirakkara et al. 2021; Seta & Federrath 2021), and allows us to compare our findings with previous studies. The turbulent acceleration field is constructed in Fourier space, which allows us to isotropically inject energy into wavenumbers, $k = |\boldsymbol{k}|$, at an effective driving scale of the turbulence on the box scale, $\ell_{\text{turb}} = L$, which corresponds to $k_{\text{turb}} = 2\pi/\ell_{\text{turb}}$. Throughout this study, we will report wavenumbers in units of k_{turb}. We drive over wavenumbers $0.5 < k < 1.5$ with a parabolic spectrum for the Fourier amplitudes, which peaks at $k = 1$, and is zero at $k = 0.5$ and $k = 1.5$.

The auto-correlation time of $\boldsymbol{F}$ is $t_{\text{turb}} = \ell_{\text{turb}}/(\mathcal{M}c_s)$, and the driving amplitude is adjusted so that the desired sonic Mach number, $\mathcal{M} = u_{\text{turb}}/c_s \approx 0.3$ is achieved in the kinematic phase of the dynamo for all of our simulations (see Table 1). As our simulations are for

subsonic turbulence, density fluctuations in all of our simulations are relatively small, with $\delta\rho/\rho_0$ of the order of 0.1–1%. Thus, ρ can be considered approximately constant, $\rho \approx \rho_0$.

2.3 Initial conditions and plasma Reynolds numbers

We initialise all our simulations with constant density, zero velocity, $\boldsymbol{u} = \boldsymbol{0}$, and zero mean magnetic field, $\boldsymbol{B}_0 = \boldsymbol{0}$, so $\boldsymbol{B} = \delta \boldsymbol{B}$. We initialise $\boldsymbol{B}$ over the largest scales in the simulation domain, $0.5 < k < 1.5$, with a parabolic profile that peaks at $k = 1$, and is zero at $k = 0.5$ and $k = 1.5$ (which is the same profile that we drive turbulence with; see the previous section). For all our simulations, we choose the initial field such that the plasma $\beta \equiv p_{\text{th}}/p_{\text{mag}} = 10^{10}$, where $p_{\text{mag}} = B^2/(8\pi)$. Seta & Federrath (2020) showed that all properties of dynamo-generated magnetic fields are not affected by the initial seed field structure or strength (as long as the field is weak).

We study simulations in the Pm ⩾ 1 regime with Re = 10–3600. All our simulations are evolved until $t/t_{\text{turb}} = 100$, well into the saturated regime of the dynamo. We test numerical convergence by using different linear grid resolutions, $N_{\text{res}} = 18, 36, 72, 144, 288$, and 576.

We run four different sets of simulations, grouped in Table 1. First, we run four simulations similar to Schekochihin et al. (2004b)[1], where Re = 10 is fixed for all simulations, and Rm is varied in order to achieve Pm ≈ 25–250. Second, we run three simulations, where we fix Re ≈ 450, and vary Rm to achieve Pm = 1, 2, and 4. Third, we run eight simulations where we fix Rm ≈ 3300, and vary Re to achieve Pm = 1–260. Finally, to test whether the dependence of k_p is on $k_{\eta,\text{theory}}$, we run four simulations where we fix $k_{\eta,\text{theory}} \approx 125$, and vary Re and Rm to achieve Pm ≈ 25–250. We report all relevant simulation parameters and derived quantities in Table 1.

Throughout this study, we use dimensionless units to describe physical quantities: ρ is in units of ρ_0, $\boldsymbol{u}$ is in units of c_s, and $\boldsymbol{B}$ is in units of $c_s \rho_0^{1/2}$. For all simulations, we set $c_s = \rho_0 = 1$. Our dissipation coefficients, ν and η, are reported in units of $\ell_{\text{turb}}^2/t_{\text{turb}}$.

3 RESULTS

3.1 Time evolution and basic properties of the turbulent dynamo

We start by comparing two representative simulation models (Re470Pm2 and Re1700Pm2), in order to highlight some of the fundamental differences in the properties of amplified magnetic fields in low- and high-Re turbulent flows, and to introduce the analysis methods that we ultimately apply to all of our simulations. However, before going into the details about how we measure important length scales of the turbulent dynamo, we first confirm that magnetic field amplifies in our simulations.

In Figure 1, we show the time evolution of the sonic Mach number, $\mathcal{M}$ (top panel), the magnetic energy, normalised by its initial value, $E_{\text{mag}}/E_{\text{mag},0}$ (middle panel), and the ratio of magnetic to kinetic energy, $E_{\text{mag}}/E_{\text{kin}}$ (bottom panel) for the Re470Pm2 and Re1700Pm2 simulations. After an initial transient period, $t/t_{\text{turb}} \approx 2$, the turbulence is fully developed (see inset in the top panel of Figure 1). We note that for MHD turbulence with a strong mean field, this transient

---

[1] Schekochihin et al. (2004b) defined the hydrodynamic Reynolds number with respect to the driving wavenumber, and thus, the Re that they report is lower than the ones we do by a factor of 2π.

Table 1. Main simulation parameters and derived quantities.

Simulation ID (1)	Re (2)	Rm (3)	Pm (4)	ν (5)	η (6)	$\mathcal{M}$ (7)	Γ (8)	$(E_{\mathrm{mag}}/E_{\mathrm{kin}})_{\mathrm{sat}}$ (9)	α_{kin} (10)	α_{mag} (11)	k_ν (12)	k_η (13)	k_P (14)
Re = 10													
Re10Pm27[†]	10	270	27	2.50×10^{-2}	1.00×10^{-3}	$0.27^{+0.05}_{-0.03}$	decaying	–	-3^{+2}_{-2}	$3.0^{+0.2}_{-0.2}$	$2.0^{+0.2}_{-0.2}$	$2.8^{+0.6}_{-0.2}$	$3.0^{+0.1}_{-0.1}$
Re10Pm54[†]	10	540	54	2.50×10^{-2}	5.00×10^{-4}	$0.27^{+0.05}_{-0.03}$	0.29 ± 0.03	$0.17^{+0.33}_{-0.07}$	-3^{+2}_{-2}	$2.9^{+0.3}_{-0.3}$	$0.30^{+0.02}_{-0.01}$	$1.1^{+0.1}_{-0.1}$	$2.7^{+0.3}_{-0.3}$
Re10Pm130[†]	10	1300	130	2.50×10^{-2}	2.00×10^{-4}	$0.26^{+0.06}_{-0.03}$	0.61 ± 0.04	$1.1^{+0.6}_{-0.3}$	-3^{+2}_{-2}	$2.8^{+0.4}_{-0.4}$	$0.28^{+0.02}_{-0.02}$	$1.8^{+0.4}_{-0.4}$	$4.0^{+0.8}_{-0.8}$
Re10Pm250[†]	10	2500	250	2.50×10^{-2}	1.00×10^{-4}	$0.25^{+0.06}_{-0.05}$	0.66 ± 0.02	$1.9^{+1.0}_{-0.5}$	-3^{+2}_{-2}	$2.7^{+0.4}_{-0.4}$	$0.30^{+0.01}_{-0.01}$	$2.2^{+0.6}_{-0.5}$	5^{+1}_{-1}
Re ≈ 450													
Re430Pm1	430	430	1	6.00×10^{-4}	6.00×10^{-4}	$0.26^{+0.07}_{-0.02}$	decaying	–	-1^{+3}_{-2}	$1.6^{+0.4}_{-0.4}$	$2.2^{+0.2}_{-0.2}$	$2.2^{+0.7}_{-0.2}$	$2.4^{+0.2}_{-0.2}$
Re470Pm2[†]	470	940	2	6.00×10^{-4}	3.00×10^{-4}	$0.28^{+0.04}_{-0.03}$	0.37 ± 0.02	$0.11^{+0.06}_{-0.04}$	-1^{+3}_{-2}	$1.7^{+0.4}_{-0.4}$	$2.2^{+0.1}_{-0.1}$	$2.9^{+0.2}_{-0.3}$	$3.4^{+0.3}_{-0.3}$
Re470Pm4	470	1900	4	6.00×10^{-4}	1.50×10^{-4}	$0.28^{+0.03}_{-0.06}$	0.69 ± 0.04	$0.2^{+0.1}_{-0.1}$	-1^{+3}_{-3}	$1.7^{+0.3}_{-0.3}$	$2.2^{+0.2}_{-0.2}$	$4.0^{+0.8}_{-0.8}$	$4.4^{+0.4}_{-0.4}$
Rm ≈ 3300													
Re3600Pm1	3600	3600	1	8.33×10^{-5}	8.33×10^{-5}	$0.30^{+0.03}_{-0.03}$	1.1 ± 0.1	$0.12^{+0.02}_{-0.02}$	-1^{+1}_{-1}	$1.9^{+0.2}_{-0.2}$	11^{+4}_{-4}	8^{+2}_{-2}	13^{+3}_{-3}
Re1700Pm2[†]	1700	3400	2	1.67×10^{-4}	8.33×10^{-5}	$0.31^{+0.04}_{-0.05}$	1.3 ± 0.1	$0.21^{+0.09}_{-0.05}$	-1^{+1}_{-1}	$1.7^{+0.2}_{-0.2}$	$6.6^{+0.4}_{-0.5}$	8^{+1}_{-1}	$9.6^{+0.8}_{-0.8}$
Re600Pm5	600	3000	5	4.17×10^{-4}	8.33×10^{-5}	$0.25^{+0.04}_{-0.03}$	1.5 ± 0.1	$0.23^{+0.09}_{-0.05}$	-1^{+3}_{-2}	$1.8^{+0.3}_{-0.3}$	$3.2^{+0.3}_{-0.3}$	6^{+2}_{-1}	7^{+2}_{-2}
Re290Pm10[†]	290	2900	10	8.33×10^{-4}	8.33×10^{-5}	$0.24^{+0.06}_{-0.03}$	1.3 ± 0.1	$0.4^{+0.2}_{-0.2}$	-1^{+2}_{-2}	$1.7^{+0.2}_{-0.2}$	$1.9^{+0.1}_{-0.1}$	$5.3^{+0.6}_{-0.6}$	$5.8^{+0.6}_{-0.6}$
Re140Pm25	140	3500	25	2.08×10^{-3}	8.33×10^{-5}	$0.29^{+0.06}_{-0.05}$	2.3 ± 0.1	$0.5^{+0.2}_{-0.1}$	-2^{+1}_{-1}	$1.8^{+0.3}_{-0.3}$	$1.3^{+0.2}_{-0.2}$	5^{+2}_{-1}	6^{+1}_{-1}
Re64Pm50	64	3200	50	4.17×10^{-3}	8.33×10^{-5}	$0.27^{+0.04}_{-0.05}$	0.93 ± 0.05	$0.9^{+0.4}_{-0.3}$	-1^{+2}_{-1}	$2.1^{+0.2}_{-0.2}$	$0.61^{+0.04}_{-0.04}$	4^{+1}_{-1}	$5.0^{+0.7}_{-0.8}$
Re27Pm130[†]	27	3500	130	1.04×10^{-2}	8.33×10^{-5}	$0.29^{+0.04}_{-0.06}$	0.98 ± 0.06	$1.4^{+0.6}_{-0.5}$	-1^{+1}_{-1}	$2.4^{+0.3}_{-0.3}$	$0.36^{+0.02}_{-0.02}$	$3.1^{+0.6}_{-0.6}$	$5.6^{+0.6}_{-0.7}$
Re12Pm260[†]	12	3100	260	2.08×10^{-2}	8.33×10^{-5}	$0.26^{+0.04}_{-0.06}$	0.89 ± 0.06	$2.0^{+1.7}_{-0.6}$	-2^{+2}_{-2}	$2.6^{+0.3}_{-0.3}$	$0.32^{+0.04}_{-0.04}$	$3.2^{+0.5}_{-0.5}$	$5.9^{+0.4}_{-0.4}$
$k_{\eta,\mathrm{theory}} \approx 125$													
Re73Pm26	73	1900	26	3.38×10^{-3}	1.35×10^{-4}	$0.25^{+0.05}_{-0.03}$	0.61 ± 0.03	$0.4^{+0.2}_{-0.1}$	-1^{+3}_{-1}	$2.1^{+0.3}_{-0.3}$	$0.67^{+0.06}_{-0.06}$	$2.5^{+0.6}_{-0.5}$	$3.9^{+0.3}_{-0.3}$
Re48Pm52	48	2500	52	5.32×10^{-3}	1.06×10^{-4}	$0.26^{+0.04}_{-0.04}$	0.81 ± 0.04	$0.7^{+0.4}_{-0.3}$	-1^{+1}_{-1}	$2.2^{+0.3}_{-0.3}$	$0.52^{+0.04}_{-0.04}$	$2.7^{+0.8}_{-0.8}$	$4.2^{+0.6}_{-0.5}$
Re25Pm140	25	3500	140	9.74×10^{-3}	7.79×10^{-5}	$0.27^{+0.03}_{-0.06}$	0.86 ± 0.04	$1.3^{+0.6}_{-0.4}$	-1^{+1}_{-1}	$2.3^{+0.3}_{-0.3}$	$0.38^{+0.03}_{-0.03}$	3^{+1}_{-1}	5^{+1}_{-2}
Re16Pm250[†]	16	4000	250	1.56×10^{-2}	6.25×10^{-5}	$0.25^{+0.04}_{-0.07}$	1.0 ± 0.1	$1.9^{+1.2}_{-0.7}$	-1^{+1}_{-1}	$2.5^{+0.3}_{-0.3}$	$0.31^{+0.04}_{-0.04}$	$3.4^{+0.7}_{-0.8}$	6^{+1}_{-2}

Note: All derived quantities (with the exception of the saturated energy) are time averaged over a subset of time realisations within the kinematic phase of the dynamo, namely, where $10^{-6} \leqslant E_{\mathrm{mag}}/E_{\mathrm{kin}} \leqslant 10^{-2}$. Columns: **(1)**: The simulation ID, where [†] indicates those simulations that have been run at a resolution of $N_{\mathrm{res}} = 576$ in addition to the default resolutions of $N_{\mathrm{res}} = 18, 36, 72, 144$ and 288 (which are common to all runs). **(2)**: The hydrodynamic Reynolds number (see Equation 1). **(3)**: The magnetic Reynolds number (see Equation 3). **(4)**: The magnetic Prandtl number (see Equation 4). **(5)**: The kinematic viscosity in units of $\ell^2_{\mathrm{turb}}/t_{\mathrm{turb}}$. **(6)**: The magnetic resistivity in units of $\ell^2_{\mathrm{turb}}/t_{\mathrm{turb}}$. **(7)**: The measured turbulent velocity (Mach number) during the kinematic phase. **(8)**: The measured growth rate, in units of t_{turb}^{-1}, of the magnetic energy during the kinematic phase. **(9)**: The measured ratio between the magnetic and kinetic energy in the saturated stage of the dynamo. In the next five columns we report the velocity and magnetic spectra power-law exponents, as well as characteristic wavenumbers measured directly from spectra (see §3.3). The wavenumbers are reported in units of k_{turb} (see §2.2). **(10)**: The measured power-law exponent for the kinetic spectra. **(11)**: The measured power-law exponent for the magnetic spectra. **(12)**: The measured viscous dissipation wavenumber. **(13)**: The measured resistive dissipation wavenumber. **(14)**: The wavenumber associated with the peak magnetic energy.

phase can take up to $t \approx 5\,t_{\mathrm{turb}}$ to become fully developed (Beattie et al. 2021), while for hydrodynamical supersonic turbulence, this time is somewhat shorter, $t \approx 2\,t_{\mathrm{turb}}$ (Federrath et al. 2010; Price & Federrath 2010). We make sure that all of our statistics are calculated from time realisations after this transient phase. We measure that $\mathcal{M}$ becomes statistically stationary at a value of $\mathcal{M} \approx 0.3$ for the Re470Pm2 and Re1700Pm2 simulations. We measure $\mathcal{M}$ for all of our simulations (see column (7) in Table 1) and find that they all lie within $\approx 10\%$ of our target $\mathcal{M} = 0.3$.

The middle panel of Figure 1 shows the evolution of the magnetic energy. We see that the initially weak seed magnetic field grows exponentially (kinematic phase), achieving more than six orders of magnitude of magnetic amplification for both of the example sim-

ulations. However, this is true for all of our simulations where we measure magnetic amplification. Throughout this study, we calculate statistics in the kinematic phase of the dynamo by averaging over all time realisations where $10^{-6} \leqslant E_{\mathrm{mag}}/E_{\mathrm{kin}} \leqslant 10^{-2}$ (indicated by the shaded grey band in the bottom panel of Figure 1). This averaging range lies within the kinematic phase for all our amplifying simulations and ensures that we measure the growth rates and fundamental length scales sufficiently far away from the initial transient phase and the saturated phase.

We find that for all our simulations where the scale separation between k_ν and k_η is fixed, an increase in Re corresponds to faster amplification of the magnetic field. This result aligns with theoretical expectations, that in the Pm $\gg$ 1 limit, for Kolmogorov (1941) turbu-
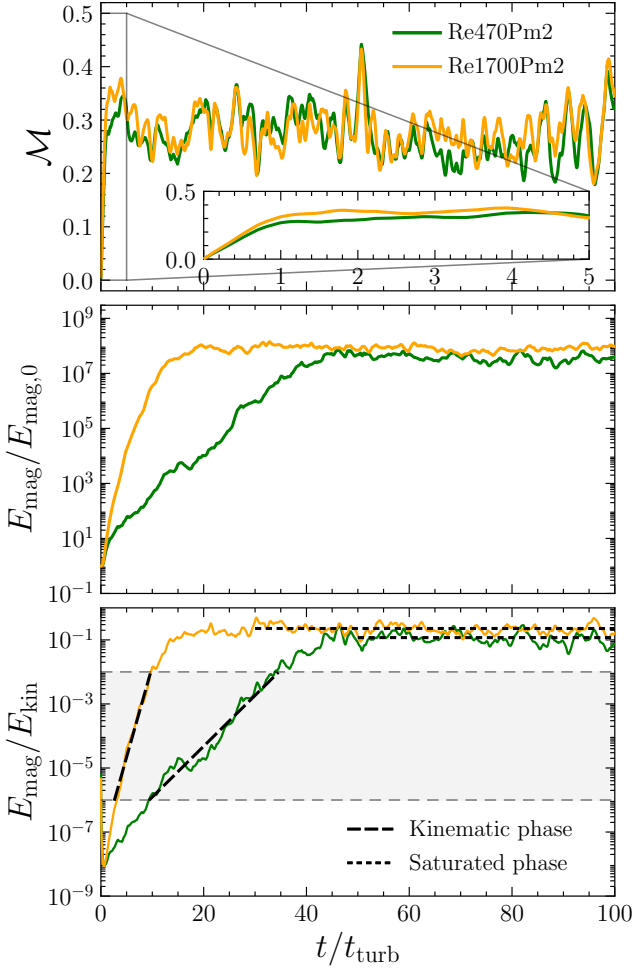
Figure 1. Time evolution of the sonic Mach number, $\mathcal{M}$ (top panel), magnetic energy normalised by the initial magnetic energy, $E_{\mathrm{mag}}/E_{\mathrm{mag},0}$ (middle panel), and the ratio of magnetic to kinetic energy, $E_{\mathrm{mag}}/E_{\mathrm{kin}}$ (bottom panel), for our Re470Pm2 (green) and Rm1700Pm2 (yellow) simulations. After an initial transient phase (see inset in the top panel), $t/t_{\mathrm{turb}} \approx 2$, the turbulence in the simulation domain is fully developed. In the kinematic phase of the dynamo, we fit an exponential function, $\exp(\Gamma\, t/t_{\mathrm{turb}})$ (dashed line), to the evolution of the energy ratio (bottom panel) over time realisations where $10^{-6} \leqslant E_{\mathrm{mag}}/E_{\mathrm{kin}} \leqslant 10^{-2}$ (indicated by the grey band). In the saturated phase of the dynamo, we measure the saturation level, $(E_{\mathrm{mag}}/E_{\mathrm{kin}})_{\mathrm{sat}}$ (dotted line). We report the growth rate, Γ, and the saturation level we measured for all of our simulations in Table 1.

lence ($u_{\mathrm{turb}} \propto \ell^{1/3}$), the growth rate scales like $\Gamma \propto \mathrm{Re}^{1/2}$ (Batchelor 1950; Kulsrud & Anderson 1992; Haugen et al. 2004a; Schekochihin et al. 2004b; Schober et al. 2012a). Bovino et al. (2013) formulated a semi-analytic model for Γ as a function of the velocity scaling exponent, ϑ, Re, and Pm. We evaluate their model for Kolmogorov (1941) turbulence, with $\vartheta = 1/3$, and find $\Gamma \approx 0.39$ for Re = 470 and $\Gamma \approx 0.98$ for Re = 1700, with Pm = 2 in both cases. From Figure 1, we measure $\Gamma = 0.37 \pm 0.02$ and 1.3 ± 0.1 for the Re470Pm2 and Re1700Pm2 simulations, respectively. Considering the overall factor of 3–4 difference in the growth rates of these two simulations, the agreement with the theoretical predictions is very good. The small differences ($\lesssim 30\%$) between the measured and predicted Γ could be the result of the implicit assumption of delta-correlated driving

in the Bovino et al. (2013) model, whereas our simulations have finite-correlated driving (see also discussion in Lim et al. 2020).

Once the magnetic field is strong enough to suppress the turbulent stretching motions (Schekochihin et al. 2004b; Seta et al. 2020; Seta & Federrath 2021), magnetic amplification slows down and reaches a final saturated state (saturated phase). We measure a statistically saturated level of $(E_{\mathrm{mag}}/E_{\mathrm{kin}})_{\mathrm{sat}} = 0.11^{+0.06}_{-0.04}$ for the Re470Pm2 simulation, and $0.21^{+0.09}_{-0.05}$ for Re1700Pm2. Thus, for these two simulations, the magnetic energy reaches $\approx$ 10–20% of the turbulent kinetic energy. For solenoidally driven turbulence, Federrath et al. (2011) provides an empirical model that predicts $(E_{\mathrm{mag}}/E_{\mathrm{kin}})_{\mathrm{sat}} = 0.44$ for $\mathcal{M} = 0.3$, Re = 1500, and Pm = 2. When we compare this with our Re1700Pm2 simulation, we find that we measure $(E_{\mathrm{mag}}/E_{\mathrm{kin}})_{\mathrm{sat}}$ that is a factor of ≈ 2 lower. This difference is likely a consequence of our simulations being driven on $k_{\mathrm{turb}} = 1$ (i.e., $\ell_{\mathrm{turb}} = L$), whereas Federrath et al. (2011) drive their turbulence on $k_{\mathrm{turb}} = 2$ (i.e., $\ell_{\mathrm{turb}} = L/2$).

While there is currently no analytical model for the saturation level that predicts $(E_{\mathrm{mag}}/E_{\mathrm{kin}})_{\mathrm{sat}}$ as a function of the plasma Reynolds numbers, current simulations suggest that the saturation level depends on Pm and Re (Schekochihin et al. 2004b; Schober et al. 2015)[2], even for supersonic turbulence (Federrath et al. 2014). Finally, we also find that our set of simulations where Re = 10 and Pm = 54–250 (see the first four runs presented in Table 1), agrees with the saturation levels that Schekochihin et al. (2004b) report for similar simulation parameters. We measure Γ and $(E_{\mathrm{mag}}/E_{\mathrm{kin}})_{\mathrm{sat}}$ for all of our simulations, and report them in columns (8) and (9) in Table 1, respectively.

3.2 Kinetic and magnetic energy structures

In Figure 2 we show two-dimensional slices of u^2/u_{rms}^2 (top panels), where u_{rms} is the root-mean-squared (rms) velocity, and B^2/B_{rms}^2 (bottom panels), where B_{rms} is the rms magnetic field, for our Re470Pm2 (left-hand panels) and Re1700Pm2 (right-hand panels) simulations. Since $\langle u \rangle = 0$ in our simulations, $u_{\mathrm{rms}} = u_{\mathrm{turb}}$. We normalise by the rms velocity and magnetic field, respectively, because we are only interested in the structure of the fields, rather than the magnitude of the fields. All four slices are taken from the middle of the box domain, $(x, y, z = L/2)$, at the time realisation where $E_{\mathrm{mag}}/E_{\mathrm{kin}} = 10^{-4}$, which corresponds to the kinematic phase of the dynamo. As discussed previously (see §2.2), the density fluctuations are small, $\rho \approx \rho_0$, in our simulations, and therefore u^2/u_{rms}^2 is proportional to $(1/2)\,\rho_0 u^2$, and hence the square of the velocity structures are equivalent to the kinetic energy structures. For the remainder of this section, we will refer to $u^2/2$ as the turbulent kinetic energy.

Visually, both the turbulent kinetic and magnetic energy densities appear to be concentrated on smaller scales in the Re1700Pm2 simulation, compared with the Re470Pm2 simulation, where Re = 1700 and 470, respectively, with Pm = 2. It is well understood that when Re increases, then the viscous scale eddies (theoretically given by Equation 2) shift to smaller scales, which increases the range of scales that the scale-free energy cascade spans (Kolmogorov 1941). For both of these simulations where Pm = 2 has been fixed, we also see that magnetic field energy densities are more concentrated on smaller scales for the higher-Re simulation. We have indicated in Figure 2

---

[2] Note that theoretically the dependence of the saturation level upon Pm and Re is a repercussion of the finite plasma parameters, and need not hold in the Pm $\to$ 0 and Pm $\to \infty$ limits.
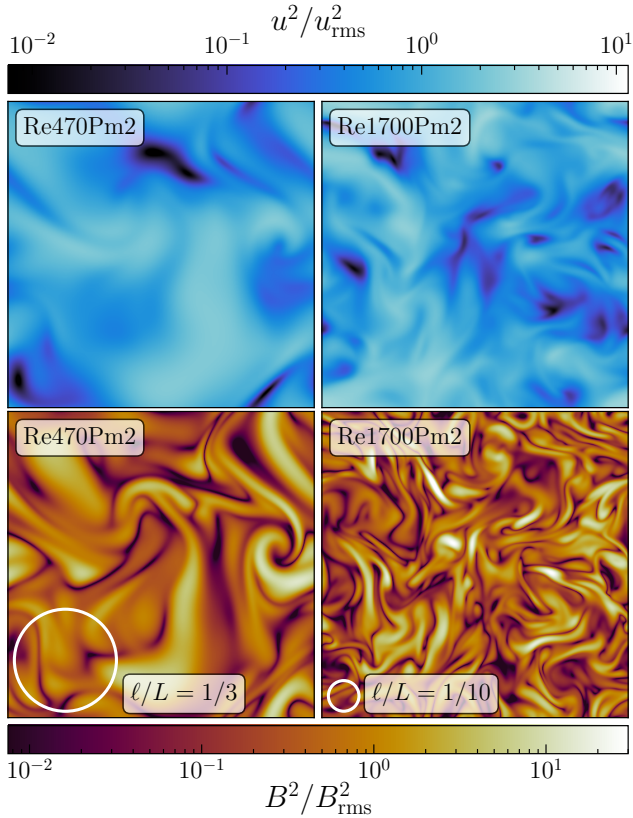
Figure 2. Two-dimensional slices taken of the u^2/u_{rms}^2 (top panels) and B^2/B_{rms}^2 (bottom panels) fields, for our Re470Pm2 and Re1700Pm2 simulations, respectively, where u_{rms} and B_{rms} are the root-mean-square of the velocity and magnetic fields, respectively. These slices are from the middle of our simulation box domain, $(x, y, z = L/2)$, at the time realisation where the energy ratio $E_{mag}/E_{kin} = 10^{-4}$. These slices have been normalised by the root-mean-squared (rms) values to reveal the morphological structures in each of the fields.

circles with radius equal to the length scale where it appears that the magnetic field energies are predominantly concentrated. Specifically, For Re470Pm2, magnetic energy appears concentrated roughly at a third of the box length, $\ell/L = 1/3$, and for Re1700Pm2 at around a tenth of the box length, $\ell/L = 10$ (in §3.3 we quantify these scales by measuring k_p in our simulations).

For both the representative simulations, the magnetic field energy density appears to be concentrated at scales smaller than the turbulent kinetic energy density. In the next section, we discuss our method for measuring fundamental length scales in both the kinetic and magnetic energy fields, including the peak scale of the magnetic field.

3.3 Kinetic and magnetic power spectra

To determine on which scale magnetic fields become most concentrated, we study the functional form of the velocity and magnetic power spectra, and characterise the spectra by measuring k_ν, k_η and k_p. This allows us to determine whether k_p depends on k_ν (Batchelor 1950) or on k_η (Kazantsev 1968; Kulsrud & Anderson 1992; Vainshtein & Cattaneo 1992; Schekochihin et al. 2002b, 2004b; Brandenburg & Subramanian 2005; Schober et al. 2015; Xu & Lazarian 2016; McKee et al. 2020).

In the kinematic phase of the dynamo, the kinetic energy is significantly greater than the magnetic energy, and the kinetic energy spectrum is largely unaffected by the magnetic spectra. In our simulations (as discussed in §2.2), fluctuations in the density field are small, and therefore the velocity power spectra are proportional to the kinetic energy spectra. In the remainder of this study, we will refer to the velocity power spectra as the kinetic energy spectra. We propose a simple model for the kinetic spectra, which is motivated by the shape of the spectrum in the kinematic phase. For Kolmogorov (1941) turbulence, the kinetic energy spectrum consists of a power law, which spans over the inertial range $k_{turb} \ll k \ll k_\nu$. Beyond k_ν, dissipation dominates, which we model with a decaying exponential function. Our model for the kinetic energy spectrum is

$$\mathcal{P}_{kin}(k) = A_{kin}\, k^{\alpha_{kin}} \exp\left(-k/k_\nu\right), \qquad (10)$$

where A_{kin} is a constant, α_{kin} is the slope of the power law in the scaling range, and k_ν is the dissipation wavenumber. Note that the expectation is $\alpha_{kin} = -5/3$ (ignoring intermittency effects, e.g. She & Leveque 1994a) for Kolmogorov (1941) turbulence, but here it is a free parameter to be determined from fits of this model to the velocity spectra of our simulations. However, in Appendix A we also test the effects of fixing $\alpha_{kin} = -5/3$ and find that it does not significantly affect our measurements of k_ν, which is the main fit parameter in this model, for the purposes of this study.

To model the magnetic power spectra, we use a solution to the Kazantsev equation (Kazantsev 1968; Brandenburg & Subramanian 2005) for the kinematic phase of the dynamo, as derived by Kulsrud & Anderson (1992). The Kazantsev model assumes an isotropic, homogeneous, Gaussian random velocity field, with zero helicity, and δ-correlation in time. The functional form of the magnetic power spectrum is given as (Kulsrud & Anderson 1992),

$$\mathcal{P}_{mag}(k) = A_{mag}\, k^{\alpha_{mag}} K_0\left(k/k_\eta\right), \qquad (11)$$

where A_{mag} is a constant, α_{mag} is the slope of the power law, and K_0 is the modified Bessel function of the second kind and order 0. The slope of the power law in the solution to the Kazantsev equation is $3/2$, but like the kinetic energy model, we retain it as a free parameter to explicitly measure the exponent in our simulations.

For all of our simulations, we fit the kinetic and magnetic spectra with Equation 10 and 11, respectively, to each time realisation where $10^{-6} \leqslant E_{mag}/E_{kin} \leqslant 10^{-2}$, corresponding to the kinematic phase of the dynamo. For each of these fits, we measure the dissipation wavenumbers, k_ν and k_η, from the fitted spectra. We also measure k_p, the peak of the magnetic power spectra, analytically by finding where the first derivative of the magnetic spectra is zero,

$$\frac{d\mathcal{P}_{mag}}{dk} \equiv A_{mag} k^{\alpha_{mag}} \left[\frac{\alpha_{mag}}{k} K_0\left(\frac{k}{k_\eta}\right) - \frac{1}{k_\eta} K_1\left(\frac{k}{k_\eta}\right)\right] = 0, \qquad (12)$$

where $K_1(x)$ is the modified Bessel function of the second kind and order 1. With the requirement that $A_{mag} \neq 0$, the only nontrivial relation for k_p that follows from this is,

$$k_p = \alpha_{mag} \frac{K_0(k_p/k_\eta)}{K_1(k_p/k_\eta)} k_\eta. \qquad (13)$$

This equation implicitly relates k_p and k_η via a constant of proportionality that involves α_{mag} and the fraction of two modified Bessel functions. Since $0 < K_0(x)/K_1(x) < 1$ for all $x > 0$, the constant of proportionality is bounded between 0 and α_{mag}.

In Figure 3, we show these spectra models fitted to the time-averaged and normalised kinetic energy spectra (top panel) and magnetic power spectra (bottom panel), for the Re470Pm2 (green) and Re1700Pm2 (yellow) simulations. We overlay our spectra fits with a black dash-dotted line, and annotate the measured k_ν, k_η and
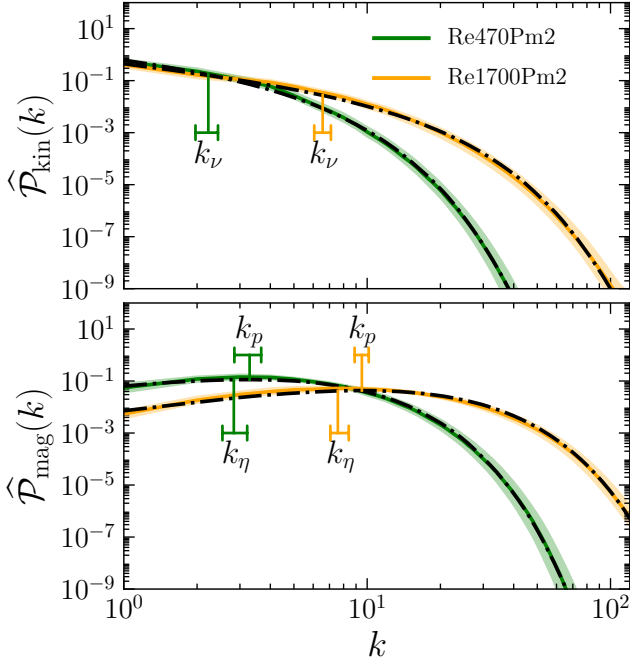
Figure 3. The normalised and time-averaged kinetic energy spectra, $\widehat{\mathcal{P}}_{\mathrm{kin}}(k)$ (top panel), and magnetic power spectra, $\widehat{\mathcal{P}}_{\mathrm{kin}}(k)$ (bottom panel), for our Re470Pm2 and Re1700Pm2 simulations. We overlay our fitted spectra models (see Equation 10 and Equation 11) shown with a black dash-dotted line, and annotate the measured dissipation wavenumbers, k_ν and k_η, as well as the peak magnetic energy scale, k_p. See columns (10) and (11) in Table 1 for the time-averaged α_{kin} and α_{mag} reported for each simulation, respectively, and columns (12 – 14) for the time averaged k_ν, k_η and k_p, respectively. We show the uncertainty of the measured scales with a bracket that spans between the 16th and 84th percentiles.

k_p, indicating the uncertainty in these scales with the width of the bracket.

As indicated in the bottom panel of Figure 3, we measure k_η on smaller wavenumbers (larger scales) than k_p for both the Re470Pm2 and Re1700Pm2 simulations. This is also true for all of our simulations (see columns (13) and (14) in Table 1). We emphasise that k_ν and k_η are characteristic wavenumbers, where the dissipation terms in our spectral models ($\mathcal{P}_{\mathrm{kin}}$ and $\mathcal{P}_{\mathrm{mag}}$, respectively) start to dominate. However, it does not mean, for example, that $\mathcal{P}_{\mathrm{mag}}(k \geqslant k_\eta) = 0$. In fact, the magnetic spectrum is typically peaked at the resistive scale, $k_p \gtrsim k_\eta$, as we will see later. Therefore, these characteristic wavenumbers are what we measure as our dissipation wavenumbers.

To ensure that the estimated scales are numerically converged with respect to the resolution of the simulation, we perform a scale convergence analysis in the next section.

3.4 Scale convergence

Before we study the dependence of k_p on k_ν and k_η, we ensure that we work with scales that have numerically converged. In this section, we present our resolution study of k_ν, k_η and k_p, and highlight this process for the Re470Pm2 and Re1700Pm2 simulations, but ultimately perform the numerical convergence study on all of our simulations. We estimate how the measured scales depend upon resolution by running all of our simulations at $N_{\mathrm{res}} = 18, 36, 72, 144$
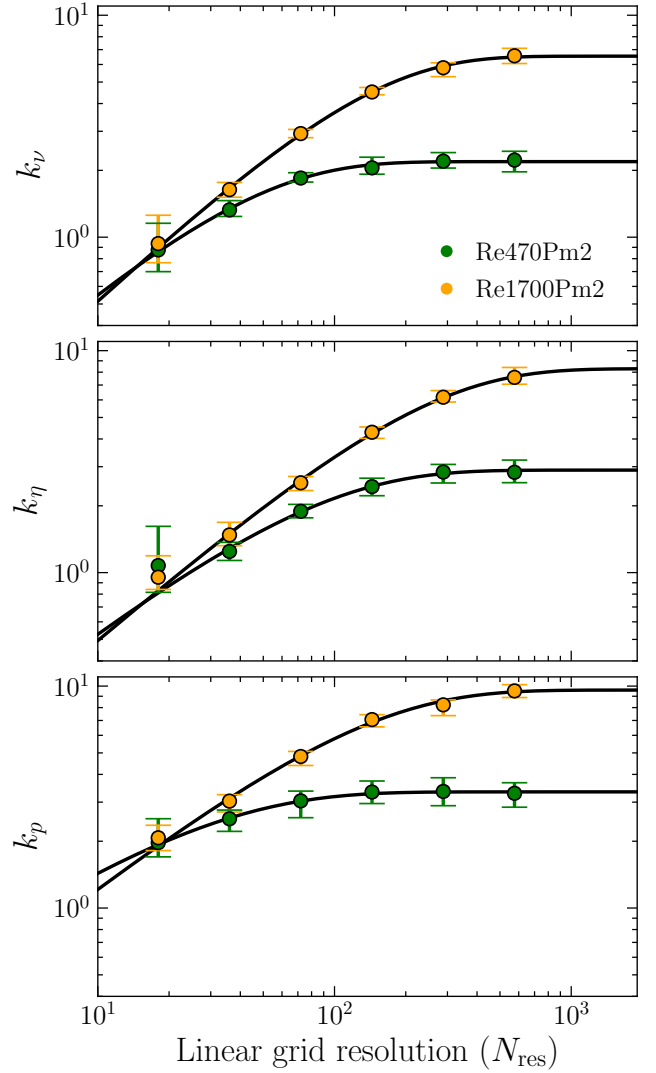

Figure 4. Measured dissipation wavenumbers, k_ν (top panel) and k_η (middle panel), and the peak magnetic field scale (bottom panel), k_p, from our Re470Pm2 and Re1700Pm2 simulations, plotted against the linear grid resolution of the simulation, N_{res}. We overlay our convergence model (see Equation 14) fitted for each of the simulations.

and 288, and some of them also at $N_{\mathrm{res}} = 576$ (indicated by † in column (1) of Table 1).

In Figure 4, we show the measured k_ν, k_η, and k_p scales for our Re470Pm2 and Re1700Pm2 simulations against N_{res} of the simulations (in the top, middle, and bottom panels, respectively). As N_{res} increases, we find that the scales we measure move to higher k-values. However, the scales start to converge at around $N_{\mathrm{res}} \approx 100$ for Re470Pm2, and ≈ 300 for Re1700Pm2. We quantify the rate of convergence, and measure the converged wavenumbers for k_ν, k_η, and k_p by fitting

$$k_{\mathrm{scale}}(N_{\mathrm{res}}) = k_{\mathrm{scale}}(N_{\mathrm{res}} \to \infty)\left\{1 - \exp\left[-(N_{\mathrm{res}}/N_{\mathrm{c}})^r\right]\right\}, \quad (14)$$

to each of the scales, for each of our simulations, where $k_{\mathrm{scale}}(N_{\mathrm{res}} \to \infty) \equiv k_{\mathrm{scale}}$ is the converged wavenumber for the simulation, N_{c} is the characteristic N_{res} where k_{scale} starts to converge, and r is the convergence rate.

We perform the convergence study for all of our simulations, and

report the fitted convergence parameters in Equation 14 for k_ν, k_η, and k_p in columns (2), (3), and (4) in Table B1, respectively. We also report the converged wavenumbers k_ν, k_η, and k_p for all of our simulations, and report them in columns (12), (13), and (14) in Table 1, respectively. From hereon, for the sake of simplicity, we will refer to the converged scales as k_ν, k_η and k_p, because we perform further analysis only with the converged scales.

3.5 Measured dissipation scales vs. theory

Here we compare the measured and converged dissipation wavenumbers, k_ν and k_η, in our simulations with those predicted from current theories, namely $k_{\nu,\text{theory}}$ (given by Equation 2) and $k_{\eta,\text{theory}}$ (given by Equation 5).

In Figure 5, we show k_ν against $k_{\nu,\text{theory}}$ (left panel), and k_η against $k_{\eta,\text{theory}}$ (right panel). We separate points on the plot into two groups: (1) those scales measured from simulations where Re < 100 (blue points), and (2) Re > 100 (red points). The reason for this separation in Re will become clearer in the next section; for now, we will calculate statistics of the measured scales for Re < 100 and Re > 100, separately.

For simulations where Re < 100, we measure that k_ν scales with $k_{\nu,\text{theory}}$ as a power law with exponent $0.51^{+0.04}_{-0.01}$, and k_η scales with $k_{\eta,\text{theory}}$ as a power law with exponent $0.83^{+0.12}_{-0.09}$. Conversely, for simulations where Re > 100, we find a linear relationship (within the 1σ uncertainty) between the theoretical and measured dissipation wavenumbers for both k_ν and k_η. Thus, we conclude that the basic dependencies of k_ν on $\text{Re}^{3/4}$, and k_η on $k_{\nu,\text{theory}}\,\text{Pm}^{1/2}$, follow the theoretical relations, but only if Re > 100. However, even if Re > 100, we find a significant shift between the measured and theoretical dissipation scales (quantified by a constant of proportionality). Fitting a linear model to the Re > 100 points, we measure that the constant of proportionality between the measured and theoretical scales for k_ν and k_η is $0.025^{+0.005}_{-0.006}$ and $0.021^{+0.002}_{-0.002}$, respectively. In summary, for Re > 100, we find

$$k_\nu = \left(0.025^{+0.005}_{-0.006}\right) k_{\text{turb}}\,\text{Re}^{3/4}, \tag{15}$$

and

$$k_\eta = \left(0.88^{+0.21}_{-0.23}\right) k_\nu\,\text{Pm}^{1/2}. \tag{16}$$

The utility of Equation 15 and 16 is that from Re and Rm, they provide the exact viscous and resistive dissipation scales, k_ν and k_η, for subsonic MHD turbulence with Pm $\geqslant$ 1.

3.6 Dependence of the peak magnetic field scale on the turbulent and magnetic dissipation scales

To determine the dependence of k_p on k_ν and k_η, we show k_p as a function of k_ν (left panel) and k_η (right panel) in Figure 6. We first consider the relationship between k_p and k_ν for simulations where Re has been fixed (see the boxes in the left-hand panel of Figure 6). Namely, there are two sets of simulations, Re $\approx$ 10 with Pm = 27–250, and Re $\approx$ 450 with Pm = 1–4. For these simulations we find that although k_ν is fixed in each set, there is an increase in k_p with Pm. This suggests that k_ν cannot be the principle quantity that controls k_p. However, we also see that there are a few data points that seem to fall along a $k_p \propto k_\nu^{1/3}$ line. While this might suggest there could be a dependence of k_p on k_ν, we will see that this is in fact not a principle dependence.

In the right-hand panel of Figure 6, we see that an increase in k_η

always results in an increase in k_p. We find that there is a dichotomy in the relationship between k_p and k_η, with k_p scaling differently with k_η for the Re < 100, compared with the Re > 100. Fitting a power law (red dashed line) to the Re > 100 data points, we measure an exponent for the power law that captures unity within the 1σ uncertainty. We measure the linear relationship between k_p and k_η for the Re > 100, shown by the solid black line.

We can now also understand that some of the simulations in the left-hand panel of Figure 6 show a correlation between k_p and k_ν. Specifically, if $k_p \propto k_\eta$ is the fundamental relation, then it follows that $k_p \propto k_\nu\,\text{Pm}^{1/2} \propto k_\nu\,\text{Rm}^{1/2}\text{Re}^{-1/2} \propto k_\nu\,\text{Rm}^{1/2}k_\nu^{-2/3} \propto k_\nu^{1/3}\,\text{Rm}^{1/2}$. Thus, if Rm is fixed, then $k_p \propto k_\nu^{1/3}$, which is exactly what we observe in the left-hand panel of Figure 6 for the Rm $\approx$ constant subclass of models (see all rows in simulation suite Rm $\approx$ 3300 and the last two rows in $k_{\eta,\text{theory}} \approx$ 125 in Table 1). However, the scaling of k_p on k_ν is simply a consequence of the fundamental underlying relation $k_p \propto k_\eta$.

This basic result agrees with current theories that predict ultimately the scale dependence of k_p in the kinematic phase of the dynamo is on k_η (Kazantsev 1968; Kulsrud & Anderson 1992; Vainshtein & Cattaneo 1992; Schekochihin et al. 2002b, 2004b; Brandenburg & Subramanian 2005; Schober et al. 2015; Xu & Lazarian 2016; McKee et al. 2020). While the relation $k_p \propto k_\eta$ was anticipated in those theories, the constant of proportionality was less clear. Using our simulation suite we measure this constant of proportionality, by fitting a linear model (black solid line in the right-hand panel in Figure 6), and find

$$k_p = \left(1.2^{+0.2}_{-0.2}\right) k_\eta. \tag{17}$$

Thus, we find that there is very little scale separation between k_p and k_η, with the peak scale located close to the resistive scale. In §3.7 we discuss the origin of the proportionality constant, $\approx$ 1.2, and its relation to the properties of the magnetic energy spectrum.

3.7 The Kazantsev exponent

In Figure 7 we show the measured power-law exponent α_{mag} in the magnetic spectra of Equation 11, from our fits in §3.3, against Re for all our simulations. We find that for simulations where Re < 100, α_{mag} increases with decreasing Re. Conversely, for simulations where Re > 100 we find that α_{mag} has reached a statistically steady value of $\alpha_{\text{mag}} = 1.7 \pm 0.1$. Recall that α_{mag}, together with the ratio of the second-order Bessel functions in Equation 13, sets the proportionality constant we measured in Equation 17. Rearranging Equation 13 gives an implicit equation for the proportionality constant, $x = \alpha_{\text{mag}} K_0(x)/K_1(x)$, where $x \equiv k_p/k_\eta$. Solving this equation with $\alpha_{\text{mag}} = 1.7 \pm 0.1$ gives a proportionality constant of 1.3 ± 0.1, which agrees with our previous measurement in Equation 17 (see the right-hand panel of Figure 6). If $\alpha_{\text{mag}} = 3/2$, as suggested by Kazantsev's theory (Kazantsev 1968; Kulsrud & Anderson 1992), then the proportionality constant would be 1.07.

Throughout this study, we have found a dichotomy between Re < 100 and Re > 100. In summary, we found that the measured dissipation wavenumbers follow a scaling consistent with theoretical predictions, and that $k_p \propto k_\eta$. Here, we also find that $\alpha_{\text{mag}} \approx$ constant. However, all of these properties are only seen if Re > 100. By contrast, the scaling relations break down for Re < 100 and α_{mag} starts to depend on Re.
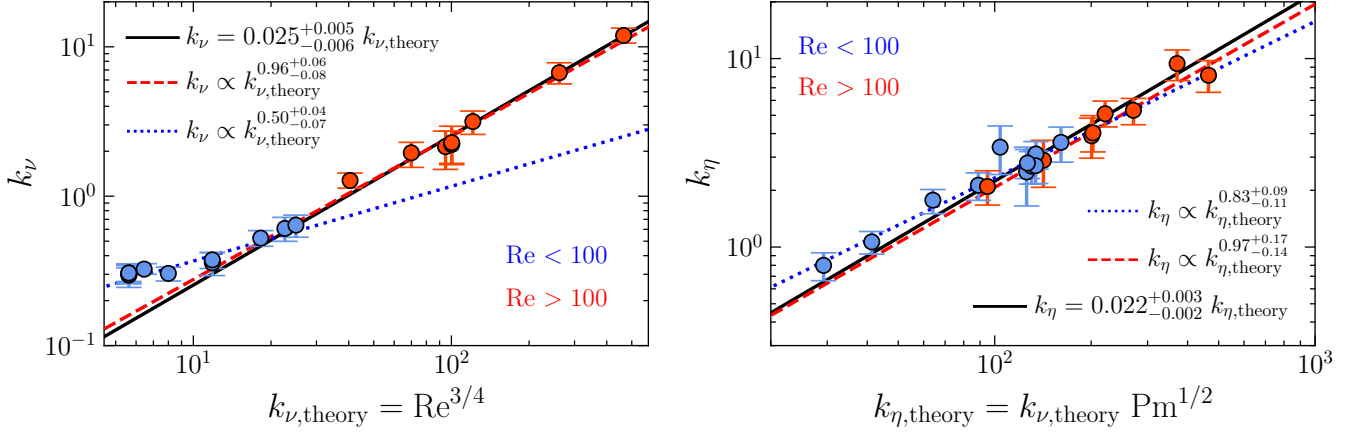
Figure 5. Measured dissipation wavenumbers, k_ν (left panel) and k_η (right panel), compared with where theoretical relations predict the dissipation wavenumbers to be (see Equation 2 and 5). The measured and theoretical scales have a different relationship for simulations where Re < 100 (blue) compared with Re > 100 (red). We fit a power law to simulation points where Re < 100 (blue dotted line), and also fit a power law model to simulations where Re > 100 (red dashed line). We finally fit a linear model to the Re > 100 points (black solid line).
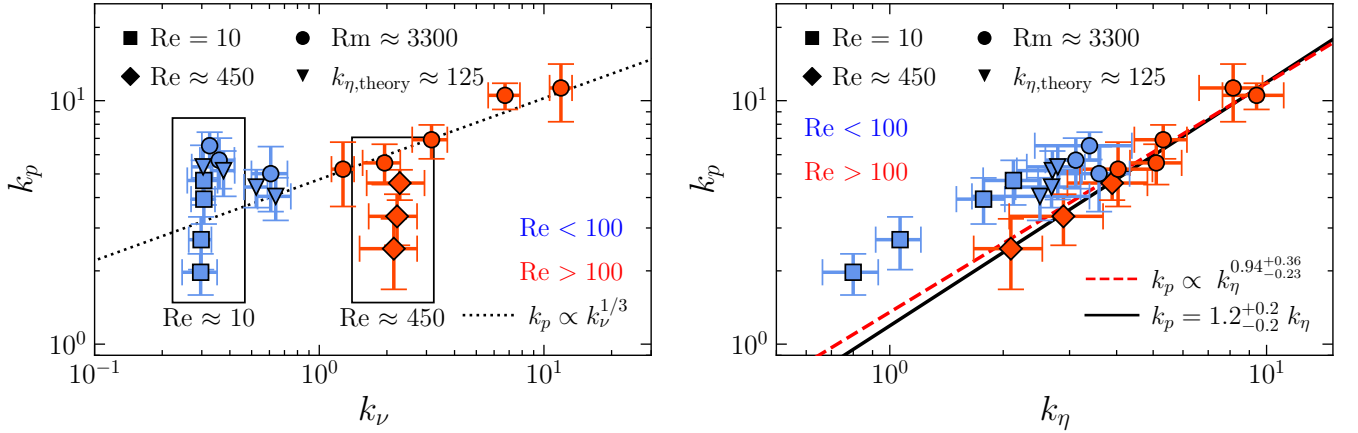
Figure 6. The measured peak magnetic field scale, k_p, plotted against the measured dissipation wavenumbers, k_ν (left panel) and k_η (right panel). We plot scales measured in simulations where Re < 100 in blue, and Re > 100 in red. In the left panel we plot a power law, $k_p \propto k_\nu^{1/3}$ (dotted line), and put a box around scales where Re ≈ 10 and 450 to highlight simulations where k_p changed, but k_ν remained constant. In the right panel we fit both a power law (red dashed line) and linear model (black solid line) to simulations where Re > 100. We report the measured power-law exponent, and the constant of proportionality for the power law and linear fits at the bottom right corner of the figure, respectively.

4 DISCUSSION

4.1 Limitations

In this paper we perform a systematic study wherein we measure k_ν, k_η, and k_p from MHD simulations (as described in §3.3) in the kinematic phase of the turbulent dynamo, and determine that the principle dependence of k_p in the subsonic, Pm ⩾ 1 regime is on k_η. To isolate the dependence of k_p on k_η, we vary the resistive scale in our simulations by changing η in Equation 8. While details of the magnetic dissipation processes can vary in nature, for example with ambipolar diffusion or Hall diffusion, where η can be a function of the magnetic field, etc., here we only considered Ohmic dissipation with constant η (i.e., we vary η between different simulations, but η is constant in space and time for a given simulation). While magnetic field dissipation may be more complex in nature, with η depending on various processes, fixing η allows us to set the magnetic Reynolds

and Prandtl number, and therefore define a controlled value of k_η, for which we can measure the dependence on Rm and Pm.

Since it is not possible to do a large parameter study, where both the inertial and sub-viscous ranges are captured in each simulation, we choose to primarily focus on the sub-viscous range. To do this, for some of our simulations, we reduce the range of scales that the inertial range occupies by choosing Re < 100. While the turbulent field produced by this driving is still random, due to the Ornstein-Uhlenbeck process, it is not entirely clear what effect the choice of the turbulent driving scale, namely $\ell_{\rm turb} = L$, has on the statistics of the turbulence. But if the correlation scale of the turbulence is approximately the driving scale, then setting the driving scale to be the entire box will reduce the independent spatial samples of the turbulence, thus making the statistics more sensitive to spatially intermittent events. Schumacher et al. (2014) showed that the velocity gradients (responsible for dissipative events in the velocity fields) in
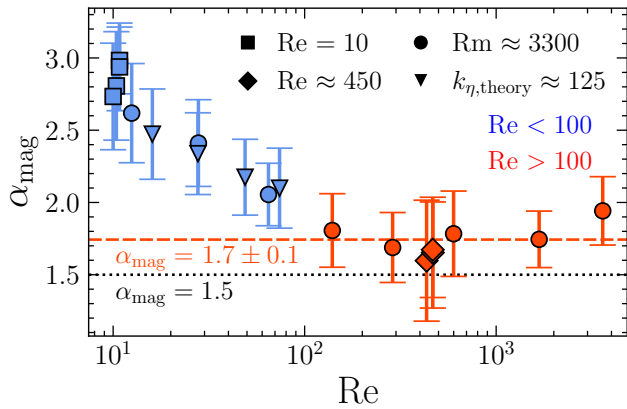
Figure 7. The magnetic power-law exponent, α_{mag} in Equation 11, measured for each of our simulations (see Table 1). We distinguish between simulations where Re < 100 (blue) and Re > 100 (red). We show the average α_{mag} for the Re > 100 simulations as a red dashed line. We also plot a reference line indicating the Kazantsev exponent, $\alpha_{\text{mag}} = 3/2$ (black dotted line).

hydrodynamical turbulent simulations transition from Gaussian to intermittent at Re ≈ 100, where intermittent fluctuations of velocity gradients are characteristic of fully-developed turbulence. It is not clear what properties differentiate our Re < 100 and Re > 100 simulations, but we hypothesise that it could be related to the intermittency of the velocity field gradients in the turbulence, as suggested by Schumacher et al. (2014) (see Appendix C for more details on the measured higher-order moments of the velocity gradients from our simulations).

In this study, we consider plasmas where Pm ⩾ 1, and while we solve the compressible MHD equations, we fix $\mathcal{M} \approx 0.3$. The astrophysical relevance of this regime is discussed in detail in the next subsection, but in many astrophysical systems, velocity fluctuations can become highly-compressible and supersonic. For example in regions of the cold interstellar medium, turbulence is compressible with $\mathcal{M} \sim 10$ (Elmegreen & Scalo 2004; Federrath et al. 2016; Beattie et al. 2019). It has been shown that compressibility affects the dynamo efficiency (see for example Haugen et al. 2004b; Federrath et al. 2011, 2014; Seta & Federrath 2021), thus further numerical experiments are necessary to understand the dependence of k_p on k_ν and k_η when the turbulence is supersonic. Moreover, it is also important to study how the dependence of k_p on k_η changes when Pm < 1, such as in the Sun's convective zone (also in planets, and in protostellar discs, where Pm ≪ 1), because if Pm < 1, then $k_\eta < k_\nu$, and it is unlikely that the scaling relations established here continue to hold.

Finally, we only study the kinematic growth phase of the dynamo. While the kinematic phase of the turbulent dynamo is responsible for amplifying weak magnetic seed fields by many orders of magnitude, inevitably, the magnetic field becomes strong enough to resist further amplification and exerts a back-reaction (via the Lorentz force) on the turbulent velocity field. This marks the transition from the kinematic phase of the dynamo to the nonlinear phase. In future works, we wish to determine whether an evolution of k_p is present in the early kinematic phase, as suggested by Schekochihin et al. (2002b); Xu & Lazarian (2016); McKee et al. (2020), and whether k_p shifts from ~ k_η to larger scales (i.e., lower k) as the dynamo transitions through the nonlinear phase to the saturated phase (Xu & Lazarian 2016; McKee et al. 2020; Galishnikova et al. 2022). This will require

very high Pm in order to maximise scale separation between k_ν and k_η, which is challenging, but may be possible with future very-high-resolution simulations. Regardless of the dynamics that take place in the nonlinear and saturated phases of the dynamo, it is clear that the kinematic phase sets the initial conditions conditions for the strength and structure of the magnetic field, where we have showed that $k_p = 1.2^{+0.2}_{-0.2} k_\eta$ in the kinematic phase.

4.2 Implications

Primordial magnetic fields must have been amplified by turbulent dynamos to the dynamically significant field strengths that we observe today (see §1 and references therein). We have explored turbulent dynamos in the Pm ⩾ 1 and incompressible regime, which holds application for magnetic fields in the early Universe, and more broadly for hot, low-density astrophysical plasmas, such as in the warm interstellar medium, accretion discs, protogalaxies, and the intracluster gas in galaxy clusters (see for example Kulsrud & Anderson 1992; Kulsrud 1999; Schekochihin et al. 2002a, 2004b; Shukurov 2004; Vazza et al. 2018; Gent et al. 2021).

Using numerical simulations, we have quantified the distribution of magnetic energy as a function of scale (modelled by Equation 11; see Kulsrud & Anderson 1992), which tells us where the magnetic energy is the strongest (i.e., the peak scale k_p) and where it dissipates (k_η). We have determined how exactly k_p and k_η depend on the hydrodynamic and magnetic Reynolds numbers (Re and Rm) of any turbulent, magnetised system (Equation 15 and 16) during the phase of the dynamo where magnetic field energy amplifies most significantly (kinematic phase of the turbulent dynamo). The implications this holds is that for a given Re and Rm, one can directly calculate k_ν (viscous wavenumber) and k_η, and determine the entire spectrum of magnetic energy via Equation 11.

In the astrophysical environments mentioned above, Re and Rm vary over many orders of magnitude (Schekochihin et al. 2007), where our results allow us to derive the distribution of magnetic energy in the kinematic phase of the dynamo taking place in these systems. For example, considering star formation in primordial halos, Schober et al. (2012b) and Nakauchi et al. (2021) calculate Re and Rm, and using these numbers, our results provide the scale-dependent magnetic energy during the kinematic phase of a turbulent dynamo. Doing this, our results imply that the magnetic energy is concentrated on scales much smaller than the size of primordial mini-halos, i.e., the field is strongest in the dense regions where accretion discs and stars form. At later stages of the dynamo (nonlinear phase of the dynamo; see the discussion at the end of §4.1), these fields can provide support against collapse and suppress fragmentation of the first-star discs, thereby reducing the number of low-mass stars that formed (Sharda et al. 2020, 2021; Stacy et al. 2022). These small-scale magnetic fields may also give rise to protostellar outflows and jets (Machida et al. 2006; Machida & Basu 2019).

Another application of our main results (Equation 15 and 16) would be to determine the effective kinematic and magnetic Reynolds numbers in ideal, incompressible MHD simulations. Since in ideal MHD simulations Re and Rm are not controlled by physical dissipation, but rather set by numerical viscosity and resistivity, one does not know the exact values of Re and Rm. Fitting Equation 10 and 11 to the kinetic and magnetic power spectra obtained in ideal MHD simulations, one is able to extract k_ν and k_η, and by inverting relations, Equation 15 and 16, one can directly calculate the effective Re and Rm for the simulations.

5 SUMMARY AND CONCLUSIONS

We have used direct numerical simulations of MHD turbulent dynamo action to measure the viscous scale (k_ν), the resistive scale (k_η), and the peak magnetic field scale (k_p), in 104 simulations with hydrodynamic Reynolds numbers $10 \leqslant \text{Re} \leqslant 3600$, and magnetic Prandtl numbers $1 \leqslant \text{Pm} \leqslant 260$ (see Table 1 and §2.3 for details of the simulations). There has been some disagreement in the literature about whether k_p should be concentrated at k_ν or k_η (see §1 and references therein). Here we determine the fundamental dependence of k_p for Pm $\geqslant 1$, which we find is on k_η, and not on k_ν. However, we also demonstrate that $k_\eta \propto k_\nu \, \text{Pm}^{1/2} \propto k_\nu^{1/3} \, \text{Rm}^{1/2}$, following theoretical predictions, and thus, in a limited parameter set where Pm or Rm had been fixed, the principle dependence of k_p on k_η could have been mistaken for a principle dependence on k_ν.

In the following, we summarise our study in item format:

• We first confirm the exponential amplification of the magnetic field during the kinematic phase of the dynamo (see Figure 1), with growth rates, Γ and magnetic-to-kinetic energy saturation levels ($E_{\text{mag}}/E_{\text{kin}})_{\text{sat}}$, that depend upon Re. We find general agreement between our measurements of Γ and ($E_{\text{mag}}/E_{\text{kin}})_{\text{sat}}$, for our simulations, compared with measurements in previous analytic and numerical works.

• In Figure 2 we show two-dimensional slices of kinetic and magnetic energy, and observe smaller-scale structures for large Re compared to small Re.

• We quantify the size of these field structures by studying the (time-averaged) kinetic and magnetic power spectra, $\mathcal{P}_{\text{kin}}$ and $\mathcal{P}_{\text{mag}}$, respectively, shown in Figure 3. We fit Equation 10 and Equation 11 to $\mathcal{P}_{\text{kin}}$ and $\mathcal{P}_{\text{mag}}$, respectively, allowing us to measure k_ν, k_η, and k_p. We make sure that these scale measurements are numerically converged (see Figure 4).

• With robust measurements of k_ν, k_η, and k_p for all of our simulations, we find that for Re > 100, there is excellent agreement in the scaling of the dissipation wavenumbers we measure from our simulations, k_ν and k_η, and the theoretical relations in the literature, $k_{\nu,\text{theory}} = k_{\text{turb}}\text{Re}^{3/4}$ and $k_{\eta,\text{theory}} = k_{\nu,\text{theory}}\text{Pm}^{1/2}$, where k_{turb} is the turbulence driving scale (see Figure 5). However, we find a significant offset by a constant factor between k_ν and $k_{\nu,\text{theory}}$, and between k_η and $k_{\eta,\text{theory}}$, respectively. We measure these two constants of proportionality, and determine the overall dissipation scale relations, $k_\nu = (0.025^{+0.005}_{-0.006}) \, k_{\text{turb}} \, \text{Re}^{3/4}$ and $k_\eta = (0.022^{+0.003}_{-0.002}) \, k_{\text{turb}} \, \text{Re}^{3/4} \, \text{Pm}^{1/2} = (0.88^{+0.21}_{-0.23}) \, k_\nu \, \text{Pm}^{1/2}$.

• We measure that k_p scales linearly with k_η (see the right-hand panel in Figure 6). For simulations with Re > 100, the relationship is $k_p = (1.2^{+0.2}_{-0.2}) \, k_\eta$. We find that the 1.2 constant of proportionality in this relationship is related to the power-law exponent α_{mag} of the magnetic power spectrum. For Re > 100, we find $\alpha_{\text{mag}} = 1.7 \pm 0.1$ (see Figure 7), slightly larger, but close to the theoretical Kazantsev exponent of 3/2.

• Throughout this study, we find that the fundamental properties of turbulent dynamo amplification break down for Re < 100. Conversely, we see good agreement between our simulations and predictions of turbulent dynamo theory for Re > 100. In this regime, our simulations have allowed us to determine the proportionality constants in theoretical relations of the turbulent dynamo, which so

far remained largely unconstrained. We conclude that Re > 100 is required for bonafide turbulent dynamo amplification, which is most likely a consequence of Re $\gtrsim$ 100 being the minimum requirement for fully-developed turbulent flow (see also work by Frisch 1995; Schumacher et al. 2014). We show in Appendix C that the universal small-scale velocity gradient statistics of turbulence changes around Re $\approx$ 100, which is in good agreement with results from Schumacher et al. (2014).

DATA AVAILABILITY

The simulation data underlying this paper will be shared on reasonable request to the corresponding author.

REFERENCES

Batchelor G. K., 1950, Proceedings of the Royal Society of London. Series A. Mathematical and Physical Sciences, 201, 405

Beattie J. R., Federrath C., Klessen R. S., Schneider N., 2019, MNRAS, 488, 2493

Beattie J. R., Mocz P., Federrath C., Klessen R. S., 2021, arXiv e-prints, p. arXiv:2109.10470

Beck R., 2001, Space Science Reviews, 99, 243

Beck R., Wielebinski R., 2018, Planets, stars and stellar systems. Oswalt TD, Gilmore G, editors, 5, 641

Boldyrev S. A., Schekochihin A. A., 2000, Physical Review E, 62, 545

Bott A. F., et al., 2021, Proceedings of the National Academy of Sciences, 118

Bouchut F., Klingenberg C., Waagan K., 2007, Numerische Mathematik, 108, 7

Bouchut F., Klingenberg C., Waagan K., 2010, Numerische Mathematik, 115, 647

Bovino S., Schleicher D. R., Schober J., 2013, New Journal of Physics, 15, 013055

Brandenburg A., Subramanian K., 2005, Physics Reports, 417, 1

Chirakkara R. A., Federrath C., Trivedi P., Banerjee R., 2021, Physical Review Letters, 126, 091103

Choudhuri A. R., 2015, Nature's Third Cycle: A Story of Sunspots. OUP Oxford

Clarke T. E., Kronberg P. P., Böhringer H., 2001, The Astrophysical Journal Letters, 547, L111

Dubey A., et al., 2008, ASP Conference Series, 385, 145

Durrer R., Neronov A., 2013, The Astronomy and Astrophysics Review, 21, 62

Elmegreen B. G., Scalo J., 2004, Annu. Rev. Astron. Astrophys., 42, 211

Eswaran V., Pope S. B., 1988, Computers & Fluids, 16, 257

Federrath C., 2013, Monthly Notices of the Royal Astronomical Society, 436, 1245

Federrath C., 2016, Journal of Plasma Physics, 82

Federrath C., Klessen R. S., Schmidt W., 2008, The Astrophysical Journal Letters, 688, L79

Federrath C., Roman-Duval J., Klessen R., Schmidt W., Mac Low M.-M., 2010, Astronomy & Astrophysics, 512, A81

Federrath C., Chabrier G., Schober J., Banerjee R., Klessen R. S., Schleicher D. R., 2011, Physical Review Letters, 107, 114504

Federrath C., Schober J., Bovino S., Schleicher D. R., 2014, The Astrophysical Journal Letters, 797, L19

Federrath C., et al., 2016, The Astrophysical Journal, 832, 143

Federrath C., Klessen R. S., Iapichino L., Beattie J. R., 2021, Nature Astronomy, 5, 365

Fletcher A., Beck R., Shukurov A., Berkhuijsen E., Horellou C., 2011, Monthly Notices of the Royal Astronomical Society, 412, 2396

Frisch U., 1995, Turbulence: The Legacy of A. N. Kolmogorov. Cambridge University Press, doi:10.1017/CBO9781139170666

Fryxell B., et al., 2000, The Astrophysical Journal Supplement Series, 131, 273

Galishnikova A. K., Kunz M. W., Schekochihin A. A., 2022, arXiv preprint arXiv:2201.07757

Gent F. A., Mac Low M.-M., Käpylä M. J., Singh N. K., 2021, The Astrophysical Journal Letters, 910, L15

Gilbert A. D., Mason J., Tobias S. M., 2016, Journal of Fluid Mechanics, 791, 568

Grasso D., Rubinstein H. R., 2001, Physics Reports, 348, 163

Han J., 2017, Annual Review of Astronomy and Astrophysics, 55, 111

Haugen N. E. L., Brandenburg A., 2004, Physical Review E, 70, 036408

Haugen N. E. L., Brandenburg A., Dobler W., 2004a, Physical Review E, 70, 016308

Haugen N. E. L., Brandenburg A., Mee A. J., 2004b, Monthly Notices of the Royal Astronomical Society, 353, 947

Jones C. A., 2011, Annual Review of Fluid Mechanics, 43, 583

Kazantsev A., 1968, Sov. Phys. JETP, 26, 1031

Kolmogorov A. N., 1941, Doklady Akademii Nauk Sssr, 30, 301

Krumholz M. R., Federrath C., 2019, Frontiers in Astronomy and Space Sciences, 6, 7

Kulsrud R. M., 1999, Annual Review of Astronomy and Astrophysics, 37, 37

Kulsrud R. M., Anderson S. W., 1992, The Astrophysical Journal, 396, 606

Lim J., Cho J., Yoon H., 2020, The Astrophysical Journal, 893, 75

Machida M. N., Basu S., 2019, The Astrophysical Journal, 876, 149

Machida M. N., Omukai K., Matsumoto T., Inutsuka S.-i., 2006, The Astrophysical Journal Letters, 647, L1

Marinacci F., et al., 2018, Monthly Notices of the Royal Astronomical Society, 480, 5113

Martins Afonso M., Mitra D., Vincenzi D., 2019, Proceedings of the Royal Society A, 475, 20180591

McKee C. F., Stacy A., Li P. S., 2020, arXiv preprint arXiv:2006.14607

Meinecke J., et al., 2015, Proceedings of the National Academy of Sciences, 112, 8211

Nakauchi D., Omukai K., Susa H., 2021, Monthly Notices of the Royal Astronomical Society, 502, 3394

Price D. J., Federrath C., 2010, Monthly Notices of the Royal Astronomical Society, 406, 1659

Rincon F., 2019, Journal of Plasma Physics, 85

Schekochihin A., Cowley S., Hammett G., Maron J., McWilliams J., 2002a, New Journal of Physics, 4, 84

Schekochihin A. A., Boldyrev S. A., Kulsrud R. M., 2002b, The Astrophysical Journal, 567, 828

Schekochihin A. A., Cowley S. C., Maron J. L., McWilliams J. C., 2004a, Physical review letters, 92, 054502

Schekochihin A. A., Cowley S. C., Taylor S. F., Maron J. L., McWilliams J. C., 2004b, The Astrophysical Journal, 612, 276

Schekochihin A., Iskakov A., Cowley S., McWilliams J., Proctor M., Yousef T., 2007, New Journal of Physics, 9, 300

Schleicher D. R., Banerjee R., Sur S., Arshakian T. G., Klessen R. S., Beck R., Spaans M., 2010, Astronomy & Astrophysics, 522, A115

Schmidt W., Federrath C., Klessen R., 2008, Physical Review Letters, 101, 194505

Schmidt W., Federrath C., Hupp M., Kern S., Niemeyer J. C., 2009, Astronomy & Astrophysics, 494, 127

Schober J., Schleicher D., Federrath C., Klessen R., Banerjee R., 2012a, Physical Review E, 85, 026303

Schober J., Schleicher D., Federrath C., Glover S., Klessen R. S., Banerjee R., 2012b, The Astrophysical Journal, 754, 99

Schober J., Schleicher D. R., Federrath C., Bovino S., Klessen R. S., 2015, Physical Review E, 92, 023010

Schumacher J., Scheel J. D., Krasnov D., Donzis D. A., Yakhot V., Sreenivasan K. R., 2014, Proceedings of the National Academy of Sciences, 111, 10961

Seta A., 2019, PhD thesis, Newcastle University, Newcastle upon Tyne, UK, http://theses.ncl.ac.uk/jspui/handle/10443/4685

Seta A., Federrath C., 2020, Monthly Notices of the Royal Astronomical Society, 499, 2076

Seta A., Federrath C., 2021, Physical Review Fluids, 6, 103701

Seta A., Bhat P., Subramanian K., 2015, Journal of Plasma Physics, 81, 395810503

Seta A., Bushby P. J., Shukurov A., Wood T. S., 2020, Physical Review Fluids, 5, 043702

Sharda P., Federrath C., Krumholz M. R., 2020, Monthly Notices of the Royal Astronomical Society, 497, 336

Sharda P., Federrath C., Krumholz M. R., Schleicher D. R., 2021, Monthly Notices of the Royal Astronomical Society, 503, 2014

She Z.-S., Leveque E., 1994a, Phys. Rev. Lett., 72, 336

She Z.-S., Leveque E., 1994b, Physical review letters, 72, 336

Sheyko A., Finlay C. C., Jackson A., 2016, Nature, 539, 551

Shukurov A., 2004, arXiv preprint astro-ph/0411739

Stacy A., McKee C. F., Lee A. T., Klein R. I., Li P. S., 2022, Magnetic fields in the formation of the first stars.–II Results (arXiv:2201.02225)

Stevenson D. J., 2010, Space science reviews, 152, 651

Subramanian K., 1997, arXiv preprint astro-ph/9708216

Subramanian K., 2016, Reports on Progress in Physics, 79, 076901

Subramanian K., 2019, Galaxies, 7, 47

Tzeferacos P., et al., 2018, Nature communications, 9, 1

Vainshtein S. I., Cattaneo F., 1992, The Astrophysical Journal, Letters, 393, 165

Vainshtein S., Zel'dovich Y. B., et al., 1972, Physics-Uspekhi, 15, 159

Vazza F., Brüggen M., Gheller C., Wang P., 2014, Monthly Notices of the Royal Astronomical Society, 445, 3706

Vazza F., Brunetti G., Brüggen M., Bonafede A., 2018, Monthly Notices of the Royal Astronomical Society, 474, 1672

Waagan K., Federrath C., Klingenberg C., 2011, Journal of Computational Physics, 230, 3331

Wagstaff J. M., Banerjee R., Schleicher D., Sigl G., 2014, Physical Review D, 89, 103001

Weiss N. O., 1966, Proceedings of the Royal Society of London. Series A. Mathematical and Physical Sciences, 293, 310

Widrow L. M., Ryu D., Schleicher D. R., Subramanian K., Tsagas C. G., Treumann R. A., 2012, Space Science Reviews, 166, 37

Xu S., Lazarian A., 2016, The Astrophysical Journal, 833, 215

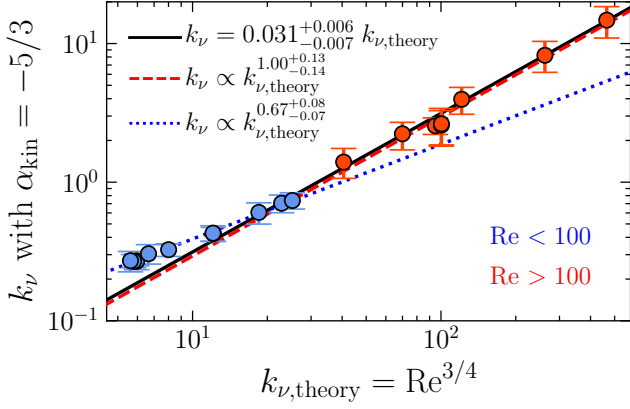Zel'dovich Y. B., Ruzmaikin A., Molchanov S., Sokoloff D., 1984, Journal of Fluid Mechanics, 144, 1

Figure A1. The same as in the left panel of Figure 5 but with the viscous dissipation wavenumber k_ν measured from the velocity spectra, Equation 10, with a fixed $\alpha_{\rm kin} = -5/3$.
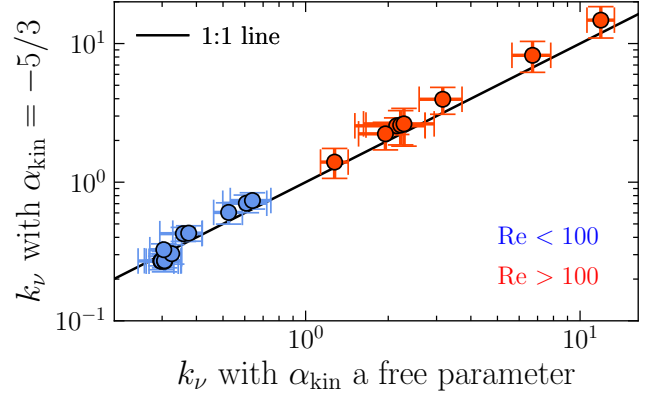

Figure A2. The viscous dissipation wavenumbers k_ν measured from fitting Equation 10 with $\alpha_{\rm kin} = -5/3$ fixed (on the y-axis), compared to fitting Equation 10 with $\alpha_{\rm kin}$ as a free parameter (on the x-axis), with a 1:1 line in solid black.

APPENDIX A: THE KOLMOGOROV EXPONENT

The limited scaling ranges in the turbulent kinetic energy spectra of our simulations (see the top panel of Figure 3) do not allow us to constrain $\alpha_{\rm kin}$ well. The main purpose of the present simulations, however, are not to measure the power-law scaling exponents of the turbulence (which requires much higher resolution; see e.g., Federrath 2013; Federrath et al. 2021); instead, we only want our simulations to capture the dissipation scales and sub-viscous range well. To confirm that the exact value of $\alpha_{\rm kin}$ does not influence our main results, here, we explore the effects of fixing $\alpha_{\rm kin} = -5/3$ in the Equation 10 model, which is the expected exponent for Kolmogorov (1941) turbulence (for simplicity, we ignore intermittency effects, which would introduce $\lesssim 10\%$ corrections to the $-5/3$ scaling exponent; see She & Leveque 1994b; Boldyrev & Schekochihin 2000; Schmidt et al. 2008), while still fitting for $A_{\rm kin}$ and k_ν. As in the main part of the study, we only fit to time realisations of the simulation where $10^{-6} \leqslant E_{\rm mag}/E_{\rm kin} \leqslant 10^{-2}$, and perform the scale convergence test discussed in §3.4 on the time-averaged k_ν values for each of our simulations.

In Figure A1, we compare the measured and converged k_ν scales from Equation 10, with $\alpha_{\rm kin} = -5/3$, for all our simulations against the scales predicted by $k_{\nu,{\rm theory}}$ (given by Equation 2). As in Figure 5, we separate points into two groups: (1) those where the simulation Re < 100, and (2) those where Re > 100. For simulations where Re < 100, we measure that k_ν scales with $k_{\nu,{\rm theory}}$ as a power law with exponent $0.67^{+0.13}_{-0.14}$ (see blue dotted line). For the Re > 100 data points, we find that fitting a power law (red dashed line) gives a linear relationship (within the 1σ uncertainty) between k_ν and $k_{\nu,{\rm theory}}$. From this, we conclude that the basic dependence of k_ν on $\mathrm{Re}^{3/4}$ still holds true for the Re > 100 data (as we had found in the left panel of Figure 5 in the main text). Moreover, by fitting a linear model (black line) to the Re > 100 data, we measure a constant of proportionality of $0.031^{+0.006}_{-0.007}$. The constant of proportionality is slightly higher compared with the constant of proportionality in the main text, $0.025^{+0.005}_{-0.006}$, where $\alpha_{\rm kin}$ was a free parameter. However, both of the constants of proportionality overlap within their 1σ uncertainties. Thus, we conclude that fixing $\alpha_{\rm kin} = -5/3$ does not significantly change the k_ν scales we measure from Equation 10.

The minor influence of $\alpha_{\rm kin}$ on the k_ν scales that we measure

is also reflected in Figure A2. We plot k_ν measured from fitting Equation 10 with $\alpha_{\rm kin} = -5/3$ fixed (on the y-axis), and compare these scales with k_ν measured by fitting Equation 10 with $\alpha_{\rm kin}$ as a free parameter (on the x-axis), as in the main part of the study. We find that the measured k_ν from the two models follow a 1 : 1 line, with k_ν slightly higher (by $\sim 20\%$) in the model where $\alpha_{\rm kin} = -5/3$. However, both methods give k_ν that agrees well with one another within the 1σ uncertainty (see column 10 in Table 1). Thus, the fact that the present simulations do not provide accurate measurements or strong constraints of $\alpha_{\rm kin}$ does not have any significant influence on the main results of this study.

APPENDIX B: FIT PARAMETERS OF THE NUMERICAL CONVERGENCE STUDY

Table B1 lists the fit parameters of the numerical scale convergence study from §3.4.

APPENDIX C: NON-GAUSSIAN COMPONENTS OF THE VELOCITY GRADIENTS

Here we provide additional evidence for our hypothesis that the intermittency of the velocity gradient field (related to the dissipative structures in the velocity) can be responsible for the Re dichotomy (see Figures 5, 6, and 7). Following Schumacher et al. (2014), we measure the kurtosis of the diagonal elements for the velocity gradient tensor, $\partial_i u_i$,

$$\mathcal{K} = \frac{\langle (\partial_i u_i)^4 \rangle_\mathcal{V}}{\langle (\partial_i u_i)^2 \rangle_\mathcal{V}^2} \tag{C1}$$

Table B1. Derived scale convergence parameters.

Simulation	k_ν		k_η		k_P	
ID (1)	N_c (2)	r	N_c (3)	r	N_c (4)	r
Re = 10						
Re10Pm27	7 ± 6	0.5 ± 0.4	20 ± 10	0.5 ± 0.5	15 ± 1	0.56 ± 0.02
Re10Pm54	9 ± 6	0.6 ± 0.5	30 ± 10	0.5 ± 0.3	27 ± 2	0.50 ± 0.04
Re10Pm130	11 ± 5	0.5 ± 0.4	80 ± 70	0.5 ± 0.3	80 ± 20	0.50 ± 0.07
Re10Pm250	11 ± 6	0.8 ± 0.7	90 ± 50	0.7 ± 0.2	83 ± 4	0.59 ± 0.02
Re $\approx$ 450						
Re430Pm1	39 ± 8	1.0 ± 0.4	40 ± 40	0.6 ± 0.6	9 ± 7	0.9 ± 0.7
Re470Pm2	38 ± 6	0.9 ± 0.3	70 ± 20	0.8 ± 0.2	22 ± 1	0.73 ± 0.06
Re470Pm4	36 ± 8	0.9 ± 0.3	$(1.1 \pm 0.5) \times 10^2$	0.9 ± 0.2	35 ± 2	0.84 ± 0.06
Rm $\approx$ 3300						
Re3600Pm1	$(2 \pm 1) \times 10^2$	1.0 ± 0.1	$(2 \pm 1) \times 10^2$	1.0 ± 0.2	$(2 \pm 1) \times 10^2$	0.77 ± 0.07
Re1700Pm2	$(1.2 \pm 0.2) \times 10^2$	1.0 ± 0.1	$(2.1 \pm 0.6) \times 10^2$	0.9 ± 0.1	$(1.1 \pm 0.1) \times 10^2$	0.84 ± 0.06
Re600Pm5	60 ± 10	0.9 ± 0.2	$(1.5 \pm 0.8) \times 10^2$	0.9 ± 0.2	90 ± 20	0.75 ± 0.06
Re290Pm10	36 ± 7	0.8 ± 0.3	$(1.4 \pm 0.4) \times 10^2$	0.9 ± 0.1	63 ± 9	0.80 ± 0.08
Re140Pm25	20 ± 10	0.5 ± 0.5	$(2 \pm 2) \times 10^2$	0.8 ± 0.2	70 ± 20	0.7 ± 0.1
Re64Pm50	5 ± 30	0.6 ± 2.4	$(1.2 \pm 0.9) \times 10^2$	0.8 ± 0.2	50 ± 9	0.73 ± 0.09
Re27Pm128	13 ± 9	0.8 ± 0.8	$(1.4 \pm 0.9) \times 10^2$	0.6 ± 0.1	84 ± 5	0.62 ± 0.02
Re12Pm260	13 ± 4	0.8 ± 0.6	$(6 \pm 3) \times 10^2$	0.5 ± 0.2	$(2.2 \pm 0.9) \times 10^2$	0.50 ± 0.03
$k_{\eta,\text{theory}} \approx 125$						
Re73Pm25	8 ± 10	0.5 ± 0.6	70 ± 40	0.8 ± 0.2	36 ± 2	0.77 ± 0.04
Re48Pm51	8 ± 23	0.7 ± 2.1	90 ± 70	0.7 ± 0.2	42 ± 3	0.71 ± 0.03
Re25Pm140	13 ± 9	1 ± 2	$(1.1 \pm 0.6) \times 10^3$	0.5 ± 0.2	69 ± 2	0.60 ± 0.05
Re16Pm250	16 ± 4	1.1 ± 0.8	$(1.4 \pm 0.7) \times 10^2$	0.6 ± 0.2	$(1.2 \pm 0.9) \times 10^2$	0.6 ± 0.1

Note: All parameters are derived from fits of Equation 14 to the time-averaged scales reported for each simulation ID (**1**) in Table 1. Next we report the characteristic grid resolution, N_c, and the convergence rate, r, measured for the viscous dissipation wavenumber, k_ν (**2**), the resistive scale, k_η (**3**), and for the peak magnetic field scale, k_P (**4**), for each simulation.

for each of the simulations in the Rm $\approx$ 3300 suite[3] (see Table 1) at $N_{\text{res}} = 288$ and time-averaged over $2t_{\text{turb}}$ within the kinematic dynamo regime. Note, in Equation C1, $\langle \cdots \rangle_\mathcal{V}$ indicates the ensemble average of some quantity within the simulation volume $\mathcal{V} = L^3$. We plot the excess kurtosis, $\mathcal{K} - 3$ (offset by the kurtosis for a Gaussian distribution, which is 3), in Figure C1, where $\mathcal{K} = 3$ corresponds to Gaussian velocity gradients (horizontal, black-dashed line).

We find the same (possibly universal) phenomena that Schumacher et al. (2014) reports, namely that the velocity gradient statistics transition from $\mathcal{K} - 3 \approx 0$ (Gaussian) to $\mathcal{K} - 3 > 0$ (super-Gaussian) at Re $\approx$ 100 (vertical, black-dashed line), in all three Cartesian directions, as is expected. Furthermore, we are able to probe simulations with lower Re than Schumacher et al. (2014) reported, and find sub-Gaussian ($\mathcal{K} - 3 < 0$) statistics in our lowest Re simulations (Re $\approx$ 12). We interpret this to mean that Re $\approx$ 100 is a transition from velocity fields having less and then more extreme dissipative events, compared with Gaussian velocity field statistics.

We note, however, that even though the transition from sub-Gaussian to super-Gaussian statistics in the velocity gradients coincides with what we call "bonafide turbulent dynamo action" (i.e., turbulent dynamo that conforms to the scale relations we explore in this study), a further, more detailed study would be required to explore this as a causal relation, which is beyond the scope of the present study. We also note that even though we report non-Gaussian velocity gradient statistics, our simulations have Gaussian velocity statistics for all Re (see Federrath 2013; Seta & Federrath 2021, for more details of the velocity statistics from our simulations).

---

[3] Note that, without the use of the numerical resolution correction method that we outline in §3.4, the Re3600Pm1 simulation is very close to the value of the numerical Re at grid resolution $N_{\text{res}} = 288$, (see Appendix C. in McKee et al. 2020, which shows that the numerical Re $\approx 2N_{\text{res}}^{4/3} \approx 3800$ for $N_{\text{res}} = 288$). In Table B1 we also find that the characteristic resolution (N_c) of k_ν, k_η and k_P exceeds the resolution of this simulation. Therefore, in Figure C1 we grey the measurements from this simulation to highlight that the effects of numerical viscosity will influence the velocity gradients we measure.
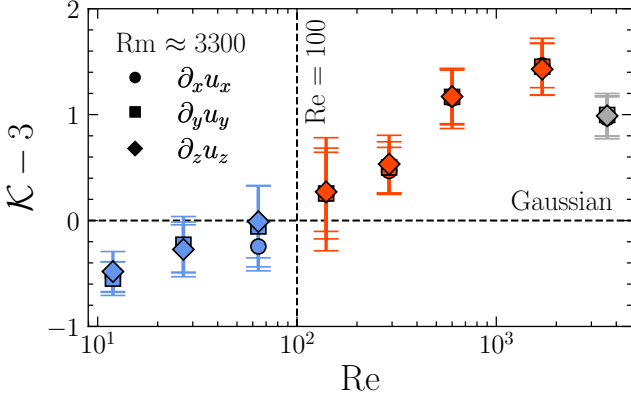
Figure C1. The excess kurtosis, $\mathcal{K} - 3$ (see Equation C1 for the definition of $\mathcal{K}$), calculated for velocity gradients, $\partial_i u_i$, measured and time-averaged over $2t_{\text{turb}}$ in the kinematic phase of the dynamo for each simulation in the $\text{Rm} \approx 3300$ simulation suite with $12 \lesssim \text{Re} \lesssim 3600$, at $N_{\text{res}} = 288$. As expected, the kurtosis values for each simulation are similar in all three directions. Here, we distinguish between simulations where $\text{Re} < 100$ (blue) and $\text{Re} > 100$ (red), as in previous Figures, but plot Re3600Pm1 in grey to indicate that numerical viscosity will influence $\partial_i u_i$ in this simulation at $N_{\text{res}} = 288$ (see footnote 3 for details). We also indicate the transitions $\mathcal{K} - 3 = 0$, which corresponds to Gaussian velocity gradients (horizontal, black-dashed line), and $\text{Re} = 100$, about which we measure that the velocity gradient statistics transition from Gaussian to super-Gaussian (vertical, black-dashed line).